

# Relative performance of body fitted and fictitious domain simulations of flow through fixed packed beds of spheres

Justin Finn\*, Sourabh V. Apte

*School of Mechanical Industrial and Manufacturing Engineering, 204 Rogers Hall, Oregon State University, Corvallis, Oregon 97331*

---

## Abstract

The relative performance of two numerical approaches involving body conforming and non-conforming grids for simulating porescale flow in complex configurations of fixed packed beds of spheres at moderate pore Reynolds numbers ( $12 \leq Re \leq 600$ ) is examined. In the first approach, an unstructured solver is used with tetrahedral meshes which conform to the boundaries of the porespace. In the second approach, a fictitious domain formulation (Apte et al., 2009. J Comput Phys 228 (8), 2712-2738) is used which employs non-body conforming Cartesian grids and enforces the no-slip conditions on the pore boundaries implicitly through a rigidity constraint force. Sphere to sphere contact points, where the fluid gap between solid boundaries becomes infinitesimal, are not resolved by either approach, but this is shown to have a negligible effect on the local flow field at the Reynolds numbers considered. Detailed grid convergence studies of both steady and unsteady flow through simple cubic packings indicate that for a fixed level of uncertainty, significantly lower grid densities may be used with the fictitious domain approach which also does not require complex grid generation techniques. This translates into large savings for simulation of flow through realistic packed beds, which is shown by both analytic estimates and actual CPU timings. The applicability of the fictitious domain approach is demonstrated by simulating unsteady flow through a randomly packed bed of 51 spheres at a pore Reynolds number of 600. The results are used to examine the dominance of helical vortices in the porescale flow field.

*Keywords:* Packed Beds, Porous Media, Fictitious Domain Approach, Body Fitted Approach

## 1. Introduction

Even at modest flow rates through porous media and packed beds, non-linear porescale flow features such as jets and vortices can have strong effects on macroscale properties of broader interest including pressure drop, heat transfer, and mass transfer. Many processes in porous media occur at lower flow rates where these inertial effects may be modeled or neglected (ie. many geologic processes). However, higher flow rates are also of importance to both natural and engineered porous systems. For example, in river and stream beds, recirculating regions can result in non-uniform nutrient and temperature distributions (Cardenas and Wilson, 2007), while higher flow rates are sometimes employed by design to increase heat transfer and reaction rates in packed bed chemical and nuclear reactors (Andrigo et al., 1999).

Flow through packed beds of spheres can be broadly classified into four regimes (Dybbs and Edwards, 1984) based on the characteristics of the porescale flow: (i) Darcy flow, where viscous forces are dominant and fluid streamlines conform to the porespace boundaries, (ii) steady, inertial flow, where boundary layers and an “inertial core” develop in the porespace, and non-linear flow features begin to emerge, (iii) unsteady inertial flow where the flow becomes time dependent but remains laminar, and (iv) turbulent flow, with chaotic velocity fluctuations and a full energy cascade. The transition from one regime to another is Reynolds number dependent, but is also very sensitive to the packing configuration and boundary conditions. This makes developing a unified understanding of porescale flows challenging, and has motivated theoretical, experimental and numerical investigations. Modern experimental techniques such as magnetic resonance imaging (MRI) (Suekane et al., 2003, Robbins et al., 2012), and particle image velocimetry (PIV) (Patil and Liburdy, 2012, Huang et al., 2008) which allow for non-invasive measurement of the porescale velocity field have been applied to study these flows. At the same time, rapidly increasing processing power has enabled highly resolved simulation (DNS/LES) techniques as viable tools to investigate the porescale flow physics at play (Hill and Koch, 2002, Magnico, 2009). In addition to

---

\*Corresponding author. Tel: 541-737-7335

*Email address:* [finnj@engr.oregonstate.edu](mailto:finnj@engr.oregonstate.edu) (Justin Finn)

providing physical insight into porescale flow behavior, DNS data sets are valuable in the process of developing lower order models for practical engineering calculations. Upscaling of the momentum equations for example, as done by Wood (2007) to predict macroscale dispersion properties, requires closures that can be obtained from three dimensional porescale velocity fields. Moving forward, it is important to continue developing efficient and accurate predictive simulation techniques capable of resolving the porescale flow field in packed beds.

Packed beds and porous media present unique challenges to resolved simulation techniques, mostly due to the complexity of the solid-fluid interface. Nonetheless, successful simulations of these flows have been carried out for laboratory scale packings containing hundreds of spheres, most often using a body fitted grid combined with a finite volume approach (Guardo et al., 2006, Atmakidis and Kenig, 2009, Dixon et al., 2006). While the body fitted approach has the ability to directly resolve the solid-fluid interface, generating and working with body conformal meshes for contacting sphere geometries can be extremely cumbersome. Most of the difficulty is due to the sphere-to-sphere contact points, which require careful treatment to avoid skewed, high aspect ratio control volumes. In our experience, the time required to generate a quality unstructured mesh for a large scale, complex geometry like a packed bed can often take longer than performing the simulation itself. Importantly, the significant meshing overhead and unstructured nature of the body fitted meshes for this problem makes systematic uncertainty quantification more difficult.

These factors leave the door open for alternative simulation approaches. The mesh related pitfalls encountered in body fitted simulations can be avoided with immersed boundary or fictitious domain approaches which use regular Cartesian grids over the entire fluid/solid domain, inclusive of the solid regions. In these types of approaches, a synthetic force is applied in or around the solid regions to satisfy the desired boundary condition (typically no-slip). The way in which this force is computed and applied is a field of active research, and a number of formulations have been proposed. A recent review on general techniques for resolved simulation of particle laden flow covering body fitted, immersed boundary, and fictitious domain approaches is given by Haeri and Shrimpton (2012), and the interested reader is referred here for a more detailed discussion. In general, immersed boundary techniques

add a corrective term to the momentum equation corresponding to a solid-fluid interaction which satisfies the no-slip condition. In the fictitious domain (or distributed Lagrange multiplier) approach, the entire domain is treated as a single fluid (inclusive of solid regions), and the rigid motion of immersed solid objects is projected in one or more steps onto the flow field using Lagrangian force points located at the solid-fluid interface.

These non body-conformal methods have evolved over the last several decades from the original works of Peskin (1972, 1977), and have been used extensively in a number of fields including fluidized beds & suspensions (Glowinski et al., 2001, Uhlmann, 2005, Simeonov and Calantoni, 2011), fluid structure interaction (Zhu and Peskin, 2002), and swimming/flying (Dong et al., 2010, Vargas et al., 2008). Not surprisingly, their broadest application has been in problems where the motion of immersed solid boundaries would require adaptive re-meshing during simulation using a body fitted approach, and application to the fixed bed type problems considered in this work has been more limited. Some notable exceptions are the recent study of transitional flow through arrays of fixed two dimensional square cylinders by Malico and Ferreira de Sousa (2012), and the study by Smolarkiewicz and Larrabee Winter (2010) of Darcy flow through reconstructed three dimensional porous media. Other alternatives to the body fitted approach exist which have been successfully applied to simulation of flows through fixed beds and porous media, including the Lattice-Boltzmann method (Hill and Koch, 2002) and methods based on smoothed particle hydrodynamics (Ovaysi and Piri, 2010).

In this paper, the performance of fictitious domain simulations of flow through packed bed geometries based on the formulation of Apte et al. (2009) is examined, relative to simulations using a well established body fitted unstructured grid approach developed from the work of Mahesh et al. (2004) with modifications to account for mesh skewness proposed by Ham and Iaccarino (2004). The main goal is to demonstrate the capability and advantages of using the former for porous media and packed bed applications, especially at moderate Reynolds numbers when it is necessary to capture complex steady and unsteady porescale flow features. In addition, it is important to establish grid density requirements when simulating large scale, complex flow problems, so that solutions can be reported with a

high level of confidence (or at least an understanding of their limitations). For example, in direct or large eddy simulations of turbulent channel flows, placing the grid cells within  $Y^+ \leq 1$  (where  $+$  denotes wall units), of the wall should produce reasonable confidence that boundary layers and small scale structures are resolved properly. This estimate takes advantage of the existence of the log-law in wall bounded flows. Likewise, for simulations of atmospheric turbulence or mixing layers, the grid spacing may be chosen to resolve the Kolmogorov scale. For inertial, transitional, and fully turbulent flows through porous media, it is not completely clear on how to estimate grid resolution requirements a priori so that all important porescale features may be captured. It is possible to estimate the net average shear stress on the porous bed by relating the net pressure drop across the bed (through for example the Ergun (1952) correlation) to the Reynolds number. Knowing the porosity, one could then compute the average shear stress and in turn estimate a boundary layer thickness. However, owing to complex bed geometries, these properties will vary substantially across the bed, and it is not clear what the grid resolution requirements are for accurate predictive simulations. Conducting grid refinement studies on very large scale simulations is also difficult due to the extensive computational cost. For this reason, our goal is to understand and establish grid resolution requirements for DNS in the steady and unsteady inertial Reynolds number regimes by performing systematic grid refinement studies of flow through porous media on smaller domains with representative packings. While random packings require careful treatment, such estimates could be a valuable starting point for estimating the computational overhead of larger scale simulations.

The remainder of the paper is structured as follows. First the surface representation, and numerical solution procedure used by both methods is discussed in Section 2. Next we examine several test cases, which are designed to test the ability of each approach for complex flows in packed beds in Section 3. Emphasis is placed on estimating the uncertainty associated with the porescale flow fields produced by each method, and determining required grid densities for acceptable confidence levels. To this end, we employ the *Grid Convergence Index* (GCI), originally proposed by Roache (1994). In Section 4, expressions for the scalability of both methods for more general, randomly packed bed simulations are

developed. Finally, in Section 5, the fictitious domain approach is used to simulate flow through a random arrangement of 51 spheres at a pore Reynolds number of 600. This case demonstrates the capability of the approach for more realistic packed bed problems of general interest and allows us to explore the porescale structure of unsteady inertial flow in a random arrangement of spheres.

## 2. Computational methods

Consider the Navier-Stokes equations for constant density and viscosity, incompressible fluid motion:

$$\nabla \cdot \mathbf{u} = 0 \quad (1)$$

$$\rho \left( \frac{\partial \mathbf{u}}{\partial t} + (\mathbf{u} \cdot \nabla) \mathbf{u} \right) = -\nabla p + \mu \nabla^2 \mathbf{u} + \rho \mathbf{g} + \mathbf{f} \quad (2)$$

where  $\rho$  is the density field,  $\mathbf{u}$  the velocity vector,  $p$  the pressure,  $\mu$  the fluid viscosity,  $\mathbf{g}$  the gravitational acceleration, and  $\mathbf{f}$  is an additional body force which is zero in the body fitted approach, and will be used to enforce rigidity within the solid phase in the fictitious domain approach. The two approaches to the solution of these equations are both implemented in a similar finite volume framework, and share several of the same basic techniques including a fractional step method (Moin and Apte, 2006), and an algebraic multigrid (AMG) solver for the pressure Poisson equation (Falgout and Yang, 2002). The codes are parallelized using Message Passing Interface (MPI), allowing for larger scale simulations by distributing the required memory over many processors.

Regardless of the approach used, precise representation of the solid-fluid interface is critical to obtain an accurate solution. Below, details are provided concerning the numerical representation of the porespace boundaries during simulation. For additional details regarding the numerical implementation, verification and validation of each method, the reader is referred to Moin and Apte (2006) and Ham and Iaccarino (2004) for the body fitted approach, and to Apte et al. (2009) for the fictitious domain approach.

## 2.1. Body fitted approach

In the body fitted approach, the pore space is first discretized into unstructured tetrahedral control volumes with a triangular surface mesh on the solid boundaries. Although arbitrarily shaped control volumes can be utilized by the solver, we have found that it is easiest to generate quality meshes in packed beds with tetrahedral cells, as opposed to other shapes (hexahedral for instance). Unstructured mesh generation for complex geometries is a non-trivial procedure in general, and in packed beds the process is complicated by sphere-to-sphere contact points, near which elements can become unmanageably small, have high aspect ratio, and be skewed. Several methods have been proposed to mitigate this problem. Most commonly, the spheres are created at reduced diameter, typically 98 or 99 percent, eliminating all contact points (Atmakidis and Kenig, 2009, Calis et al., 2001, Nijemeisland and Dixon, 2004), and creating a small gap between spheres. A related approach first pursued by Guardo et al. (2006) is to create the spheres slightly larger than they actually are, so that they overlap, creating a continuous edge in the plane perpendicular to the contact line. Magnico (2003, 2009) has used a structured grid approach where the surface representation is stair stepped due to a voxelized treatment of the solid boundaries. While the meshing overhead is low with this approach, an artificial surface roughness is imposed, even with significantly refined grids. The approach which is pursued here takes advantage of the fact that the fluid very close to the solid contact points tends to be more or less stagnant even at moderate Reynolds numbers. In light of this, Kuroki et al. (2009) have proposed a *bridge method*, wherein they do not change the diameter of the sphere, but rather unite two contacting spheres with a cylinder placed on the contact line as shown in Figure 1. This technique has the potential to significantly reduce overall mesh size because the regions where small element sizes are required have been eliminated. Nelson (2009) extended this technique, and created a smooth fillet between the two contacting surfaces allowing for more continuity in the surface mesh for the application of prismatic surface layers.

The bulk behavior of flows in porous media and packed beds is strongly affected by porosity, so it is important that the bridges do not add significant solid volume to the

porespace. The overall *increase in solid volume* due to a single bridge can be shown to be

$$\mathcal{V}_b = \frac{\pi}{8} D_b^2 \left( D - \sqrt{D^2 - D_b^2} \right) - \frac{\pi}{12} \left( D - \sqrt{D^2 - D_b^2} \right)^3 \quad (3)$$

In this work, the bridge diameter is chosen to be  $D_b = 0.25D$ , so the volume of a single cylinder bridge is  $\mathcal{V}_b = 0.0015\mathcal{V}_{sp}$ , where  $\mathcal{V}_{sp}$  is the volume of a single sphere. Thus, even for packings with moderate coordination numbers, we can expect the total solid volume to increase by less than 1% (and only in the mostly stagnant contact regions). By comparison, the more common technique of shrinking the spheres to 99% of their original size will decrease the solid volume (everywhere) by roughly 3%.

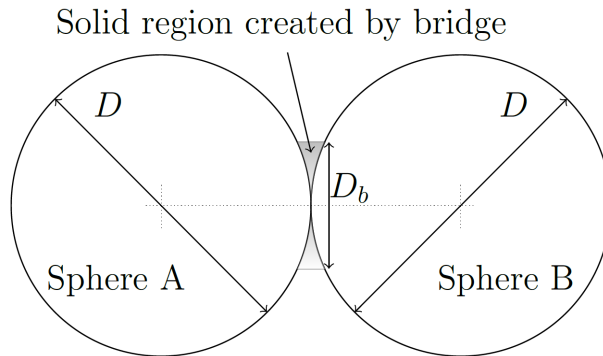


Figure 1: Schematic of the cylinder bridge created between two contacting spheres.

It quickly becomes challenging and time consuming to generate this type of geometry and mesh for more than a few spheres using the GUI of a typical mesh generation package because of the large number of geometric entities and high surface area to volume ratio. In light of this, a parameterized and automated approach has been developed that takes advantage of the commercial meshing package Pointwise's® full TCL-TK programmability. All sphere-sphere or sphere-boundary contact points are bridged, then trimmed and joined into a single watertight model. Once the solid geometry is assembled, a triangular surface mesh is generated on all solid surfaces. Because of the complex arrangements encountered in porous media, uniform mesh spacing,  $\Delta = \mathcal{V}_{cv}^{1/3}$ , where  $\mathcal{V}_{cv}$  is the cell volume is used everywhere in the porespace. In geometries with entry/exit regions, mesh coarsening is used to reduce the total mesh size. An example of the cylinder bridge geometry and surface mesh

is shown in the lower half of Figure 2 for a simple two sphere system. This meshing tool is robust and can handle arbitrary random or arranged packings of spheres contained in box or tube geometries. It has been used to generate meshes with over 80 million control volumes and for geometries containing over 500 spheres. The interested reader is referred to Finn and Apte (2012) for examples.

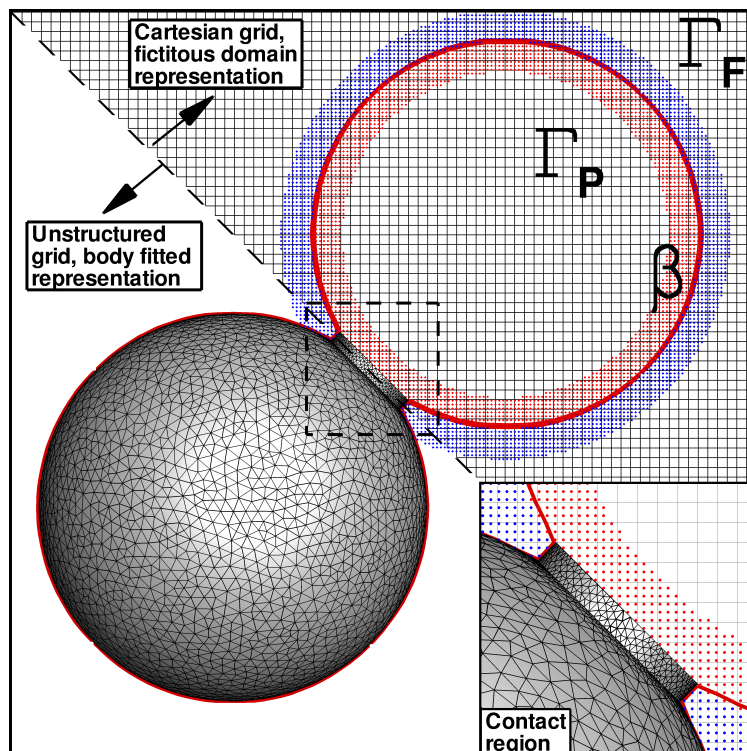


Figure 2: Comparison of discrete surface representations used by the body fitted (bottom) and fictitious domain (top) approaches.

## 2.2. Fictitious domain approach

The computations carried out with the fictitious domain approach utilize a hybrid Lagrangian-Eulerian (HLE) formulation for representation of arbitrarily shaped immersed solid objects and is not limited to the spherical objects used here. Although we consider only fixed beds, this fictitious domain approach also allows accurate representation of either forced or freely moving boundaries embedded in the flow and is easily extensible to fluidized bed simulations. Let  $\Gamma$  be the the entire computational domain which includes both the

fluid ( $\Gamma_F$ ) and the solid particle ( $\Gamma_P$ ) domains shown in upper half of Figure 2. Let the fluid boundary not shared with the solid be denoted by  $\beta$  and have a Dirichlet condition (generalization of boundary conditions is possible). The basis of a fictitious domain approach is to extend the Navier-Stokes equations for fluid motion over the entire domain  $\Gamma$  inclusive of immersed solids (Glowinski et al., 2001). The natural choice for these fixed bed problems is to assume that the immersed solid region,  $\Gamma_P$ , is filled with the same Newtonian *fluid* with density ( $\rho$ ) and viscosity ( $\mu$ ) as  $\Gamma_F$ . Both the real and fictitious fluid regions will be assumed as incompressible and thus equations 1 and 2 apply everywhere in the domain. In addition, as the immersed solids are assumed rigid, the motion of the material inside  $\Gamma_P$  is constrained to rigid body motion. Several ways of obtaining the rigidity constraint have been proposed (Glowinski et al., 2001, Patankar and Joseph, 2001, Sharma and Patankar, 2005). We follow the formulation developed by Sharma and Patankar (2005) and described in detail by Apte et al. (2009). A brief description is given here for completeness. The solid fluid interface,  $\beta$ , is located on the Cartesian grid with subgrid scale marker points as shown in the top half of Figure. 2. These marker points carry a color function indicating the relative location of the interface, and remain fixed during the simulations.

In order to enforce that the material inside the immersed solid remains rigid, a constraint is required that leads to a non-zero forcing function,  $\mathbf{f}$ . Inside the solid region, the rigid body motion,  $\mathbf{u}^{RBM}$ , implies vanishing deformation rate tensor:

$$\left. \begin{aligned} \frac{1}{2} \left( \nabla \mathbf{u} + (\nabla \mathbf{u})^T \right) = \mathbf{D}[\mathbf{u}] = 0, \\ \Rightarrow \mathbf{u} = \mathbf{u}^{RBM} = \mathbf{U} + \Omega \times \mathbf{r} \end{aligned} \right\} \text{ in } \Gamma_P, \quad (4)$$

where  $\mathbf{U}$  and  $\Omega$  are the translation and angular velocities of the object and  $\mathbf{r}$  is the position vector of a point inside the object from its centroid. For the fixed bed problems considered here,  $\mathbf{u}^{RBM}$  is always zero. The vanishing deformation rate tensor for rigidity constraint automatically ensures the divergence free, incompressibility constraint inside the solid region. The incompressibility constraint gives rise to the scalar field (the pressure,  $p$ ) in a fluid. Similarly, the tensor constraint  $\mathbf{D}[\mathbf{u}] = 0$  for rigid motion gives rise to a tensor field inside the solid region. Distributed Lagrange multipliers based approaches have been proposed

to solve for the rigid body motion and impose the rigidity constraint which requires an iterative solution strategy. Sharma and Patankar (2005) proposed an approach that provides the rigidity constraint explicitly, thus reducing the computational cost significantly. Noting that the tensorial rigidity constraint can be reformulated to give:

$$\nabla \cdot (\mathbf{D}[\mathbf{u}]) = 0 \text{ in } \Gamma_P \quad (5)$$

$$\mathbf{D}[\mathbf{u}] = 0 \text{ on solid/fluid interface, } \beta \quad (6)$$

A fractional-step algorithm can be devised to solve the fictitious domain problem (Patankar and Joseph, 2001, Sharma and Patankar, 2005, Apte et al., 2009). Knowing the solution at time level  $t^n$  the goal is to find  $\mathbf{u}$  at time  $t^{n+1}$ .

1. In the first step, the rigidity constraint force  $\mathbf{f}$  in equation 1 is set to zero and the equation together with the incompressibility constraint (equation 4) is solved by standard fractional-step schemes over the entire domain. Accordingly, a pressure Poisson equation is derived and used to project the velocity field onto an incompressible solution. The obtained velocity field is denoted as  $\mathbf{u}^{n+1}$  inside the fluid domain and  $\hat{\mathbf{u}}$  inside the solid object.
2. To solve for  $\mathbf{u}^{n+1}$  inside the solid region we require  $\mathbf{f}$ . The constraint on the deformation rate tensor given by equation 4, along with the no-slip specification at the solid-fluid interface can be reformulated to obtain:

$$\nabla \cdot (\mathbf{D}[\mathbf{u}^{n+1}]) = \nabla \cdot \left( \mathbf{D} \left[ \hat{\mathbf{u}} + \frac{\mathbf{f}\Delta t}{\rho} \right] \right) = 0; \quad (7)$$

$$\mathbf{D}[\mathbf{u}^{n+1}] \cdot \mathbf{n} = \mathbf{D} \left[ \hat{\mathbf{u}} + \frac{\mathbf{f}\Delta t}{\rho} \right] \cdot \mathbf{n} = 0. \quad (8)$$

The velocity field in the solid is zero for fixed beds. Thus  $\hat{\mathbf{u}}$  is split into a rigid body motion ( $\mathbf{u}^{RBM} = \mathbf{U} + \Omega \times \mathbf{r} = 0$ ) and residual non-rigid motion ( $\mathbf{u}'$ ). The above formulation can be easily generalized to solid bodies with *specified motion* by directly setting  $\mathbf{u}^{RBM}$  to the specified velocity.

3. The rigidity constraint force is then simply obtained as  $\mathbf{f} = \rho(\mathbf{u}^{RBM} - \hat{\mathbf{u}})/\Delta t$ . This sets  $\mathbf{u}^{n+1} = \mathbf{u}^{RBM}$  in the solid domain. Note that the rigidity constraint is non-zero

only inside the solid domain and zero everywhere else. This constraint is then imposed in a third fractional step.

The utility of the Lagrangian marker points (see Figure 2) is in locating the solid/fluid interface and enforcing the boundary condition on  $\beta$  with subgrid scale resolution in the above steps. A quantity can be defined and calculated at the marker points (for example  $\mathbf{f}$ ) and then be projected onto the Eulerian grid, or vice-versa, using accurate interpolation kernels (Roma et al., 1999). In practice, because the no-slip condition at the boundary of the porespace is enforced indirectly, the precision of the boundary location is directly linked to the grid resolution. This is especially true near regions of sharp boundary curvature such as sphere to sphere contact points. This is illustrated in the top half of Figure 2 where the solid line denotes the fictitious domain solid-fluid interface. Even with subgrid marker points, the high curvature contact region appears as a *bridge* similar to the one obtained (intentionally) in the body fitted meshing procedure.

### 2.3. Uncertainty Estimation

In the absence of an analytic solution, it is important to be able to estimate and report the uncertainty associated with a CFD calculation. Furthermore, uncertainty should be computed in a consistent manner, which can be compared by future workers using new or different simulation approaches. For this reason, we choose the *grid convergence index* (GCI), originally proposed by Roache (1994), to quantify the uncertainty associated with some of our simulation results. The GCI is based on the ideas of Richardson extrapolation and does not rely on the existence of an exact solution or the assumption that a very fine grid solution may be taken as such. It is robust as a general post-processing tool for error estimation, and has proven its utility for numerical solutions of a variety of different flows (Cadafalch et al., 2002).

To compute an uncertainty band for the flow variable,  $\phi$ , the solution is first obtained on at least three grids with (not necessarily equal) refinement ratios  $r_{21} = \Delta_2/\Delta_1$  and  $r_{32} = \Delta_3/\Delta_2$ . For the purposes of comparing results which utilize control volumes with various shapes, we define the grid spacing in this paper as  $\Delta = \mathcal{V}_{cv}^{1/3}$ , where  $\mathcal{V}_{cv}$  is the average

cell volume. For nominally two dimensional cases (such as Section 3.1), the analog to this definition is  $\Delta = A_{cv}^{1/2}$ , where  $A_{cv}$  is the cell area. The fine and medium grid solutions,  $\phi_1$  and  $\phi_2$ , are then interpolated to the coarse grid, where the variations,  $\epsilon_{32}(\mathbf{x}) = \phi_3(\mathbf{x}) - \phi_2(\mathbf{x})$ , and  $\epsilon_{21}(\mathbf{x}) = \phi_2(\mathbf{x}) - \phi_1(\mathbf{x})$ , are computed. From  $\epsilon_{32}(\mathbf{x})$  and  $\epsilon_{21}(\mathbf{x})$ , the *local* apparent order of accuracy,  $\mathcal{P}(\mathbf{x})$ , may be calculated, using the following equation (Celik et al., 2008).

$$\mathcal{P}(\mathbf{x}) = \frac{1}{\ln(r_{21})} \left| \ln |\epsilon_{32}(\mathbf{x})/\epsilon_{21}(\mathbf{x})| + \ln \left( \frac{r_{21}^{\mathcal{P}(\mathbf{x})} - \text{sign}(\epsilon_{32}/\epsilon_{21})}{r_{32}^{\mathcal{P}(\mathbf{x})} - \text{sign}(\epsilon_{32}/\epsilon_{21})} \right) \right| \quad (9)$$

In the event that  $r_{21} \neq r_{32}$ , a straightforward iteration of equation 9 can be used to determine  $\mathcal{P}(\mathbf{x})$ . The global order of convergence,  $\mathcal{P}_G$ , is then computed by averaging  $\mathcal{P}(\mathbf{x})$  at nodes where monotone convergence is observed, indicated by  $\text{sign}(\epsilon_{32}/\epsilon_{21}) > 0$ . The percentage of nodes exhibiting monotone convergence is denoted  $\%M_n$  and indicates the degree to which the results are in the asymptotic regime. Non-monotone grid convergence of CFD solutions is an unfortunate reality, and is not necessarily cause for excessive concern (Eça et al., 2005). Using the global order of convergence, the *GCI* of the fine grid solution is then computed as

$$GCI(\mathbf{x}) = F_s \left| \frac{\phi_1(\mathbf{x}) - \phi_2(\mathbf{x})}{1 - r_{21}^{\mathcal{P}_G}} \right| \quad (10)$$

where  $F_s = 1.25$  is a reasonably conservative factor of safety for a three grid refinement study (Roache, 2003). In this form, the *GCI* has the same units as  $\phi$ , and may be taken as a local uncertainty band. Alternatively, it may be multiplied by  $100/\phi_{ref}$ , where  $\phi_{ref}$  is some meaningful reference value, to obtain a dimensionless percent relative uncertainty. In this work we will report the global uncertainty,  $GCI_G$ , as the node averaged percent relative uncertainty with  $\phi_{ref}$  equal to the spatial average of  $RMS(\phi(\mathbf{x}))$ . Boundary nodes, or nodes where  $\phi$  is fixed (such as within rigid bodies in fictitious domain computations), are excluded from the global averages. Finally, the grid resolution required to obtain some target level of uncertainty, denoted  $GCI^*$ , may be estimated as (Roache, 1997)

$$\Delta^* = \Delta_1 \cdot \left( \frac{GCI^*}{GCI_G} \right)^{1/\mathcal{P}_G} \quad (11)$$

This is useful for determining simulation size requirements as is done in Section 4.

### 3. Performance assessment

The test cases examined here are designed to provide a basis for quantifying the performance of our two methods for fixed bed flow simulations. First, the influence of grid type and quality on solution error in the absence of solid boundaries is demonstrated using the case of decaying Taylor vortices. Second, as a basic hydrodynamic validation for packed bed and porous media flows, we examine Stokes flow through a dilute periodic array. Third, to test the effect of sphere to sphere contact points on both the body fitted and fictitious domain approaches, flow past a contacting pair of spheres is simulated. Finally flow through a simple cubic lattice is considered at both steady and unsteady Reynolds numbers. This serves two purposes. First, the predicted porescale velocity profiles can be compared to those measured experimentally by Suekane et al. (2003). Second, the geometry is simple enough to allow a detailed grid refinement study from which we can generate error estimates, and determine the scalability of each approach for larger packed bed simulations over a broad range of pore Reynolds numbers.

#### 3.1. Baseline accuracy and mesh quality: Decaying Taylor vortices

Based on the numerical implementations, in the absence of immersed solids the fictitious domain and body fitted approaches are identical. An important first step in understanding the solution behavior in complex packed bed flows is to assess the influence of grid type and quality on solution accuracy in the absence of solid boundaries. To accomplish this, we examine the case of decaying Taylor vortices (Taylor, 1923). This time dependent solution to the Navier-Stokes equations can be written as:

$$u_x = -\cos(\pi x) \sin(\pi y) \exp^{-\frac{2\pi^2 t}{Re}} \quad (12)$$

$$u_y = \sin(\pi x) \cos(\pi y) \exp^{-\frac{2\pi^2 t}{Re}} \quad (13)$$

$$p = -\frac{1}{4} (\cos(2\pi x) \cos(2\pi y)) \exp^{-\frac{4\pi^2 t}{Re}} \quad (14)$$

We assign the initial condition at time  $t = 0$  for  $Re = 10$  in a periodic domain with  $-1 < x < 1$ ,  $-1 < y < 1$  on the three families of grids shown in Figure 3: (a) uniform,

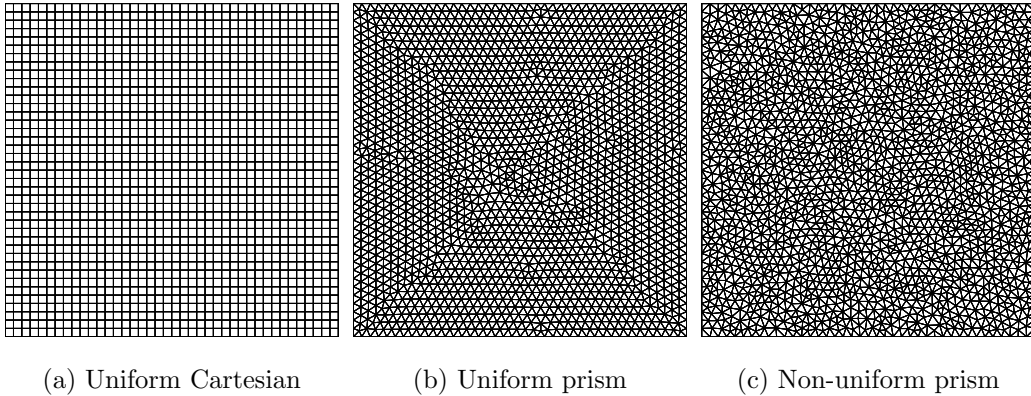


Figure 3: Three families of grids used in the Taylor vortex case.

Cartesian grids with cubic control volumes, (b) prism grids with nearly uniform element size and aspect ratio near 1, (c) prism grids with non-uniform element size and aspect ratio. The vortex decay is simulated up to a time  $t = 0.2$  on grids with average cell edge lengths of  $l_e = 0.1, 0.05, 0.025$ . This results in grid spacing,  $\Delta = A_{cv}^{1/2} = l_e$  for the Cartesian grids, and  $\Delta \approx 0.66l_e$  for the prism grids. At the end of the simulation, the error in the  $u_x$  velocity component is computed at each cell center using equation 12. A constant time step,  $\Delta_t = 2.5 \times 10^{-3}$ , is used to isolate the spatial discretization errors, resulting in a maximum CFL number of  $CFL = \|\mathbf{u}\|\Delta_t/\Delta = 0.15$  for the initial condition on the finest prism grid. Figure 4 shows the  $L_1$  and  $L_{max}$  error norms as a function of grid spacing for the three families of grids. As expected, the Cartesian grids show perfect second order spatial accuracy. Second order accuracy in the  $L_1$  norm is retained by the uniform prism grids, but the  $L_{max}$  norm shows a significant increase in *local* error, which underscores the sensitivity of the methods to local grid quality. The convergence of error on the non-uniform prism grids is only slightly better than first order in both the  $L_1$  and  $L_{max}$  norms, and the magnitude of solution error is nearly 1 order of magnitude greater than the Cartesian grids. This demonstrates that unstructured meshes with lower quality cells compared to Cartesian grids can introduce significant local solution errors. This is important to consider for packed beds, where irregular geometries make generating uniform triangular/tetrahedral cells very difficult

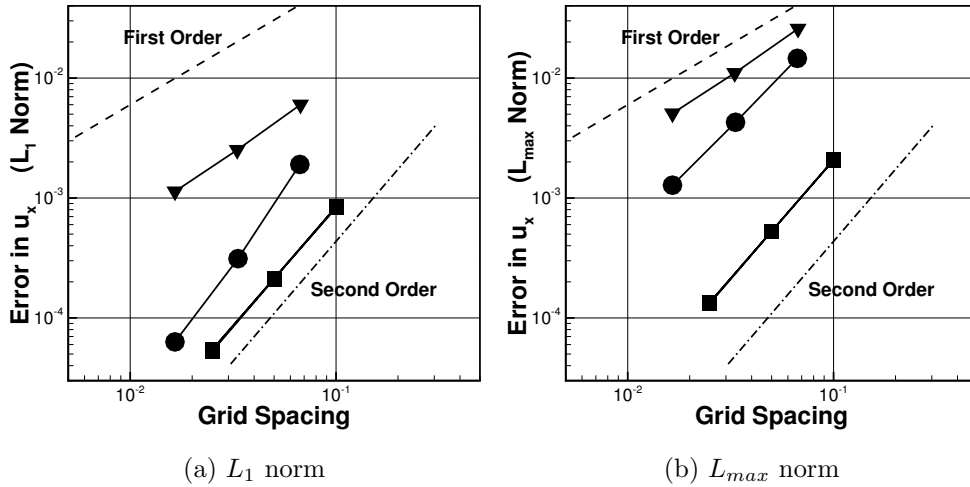


Figure 4:  $L_1$  and  $L_{max}$  error norms for the  $u_x$  velocity component. Cartesian  $\blacksquare$ , uniform prism  $\bullet$ , non-uniform prism  $\blacktriangledown$ .

### 3.2. Basic hydrodynamic verification: Stokes flow drag on a single sphere in a dilute array

To begin testing these approaches in packed bed type applications, we examine the case of Stokes flow through a dilute periodic array of spheres. The geometry we consider is a periodic box, with all sides of length  $L$  which contains a single sphere with diameter,  $D$ , centered at  $\mathbf{x} = L/2$ . The periodicity in all directions allows us to represent an infinite simple cubic arrangement with a single sphere. The ratio  $L/D$  is chosen to be 2.015 to allow for comparison with the integral equation solutions of Zick and Homay (1982) for the relatively dilute solid volume fraction of  $(1 - \epsilon) = 0.064$ , where  $\epsilon$  is the fluid void fraction. Three Cartesian and tetrahedral grids are created with  $D/\Delta = 12, 24, 48$ , where  $\Delta = \mathcal{V}_{cv}^{1/3}$ .

The flow is started from rest, and accelerated by applying a small, uniform pressure gradient everywhere. When the flow reaches equilibrium, we confirm that the pore Reynolds number is small enough that inertial effects are negligible, and the total force exerted on the sphere is then computed. For this case,  $Re_p = \frac{U_p D}{\nu} \approx 1 \times 10^{-3}$  where  $U_p$  is the average velocity in the fluid region of the porespace, or *pore velocity*. In the fictitious domain approach, the drag force,  $f_d$ , is taken to be the component of the rigid body force aligned with the applied pressure gradient. In the body fitted approach, the drag force is obtained

by integrating the surface stress over the sphere boundary faces. This is then normalized by the Stokes drag on a single sphere in unbounded flow to obtain the drag coefficient,  $C_D$ .

$$C_D = \frac{f_d}{N_{sp}3\pi\mu DU_p\epsilon} \quad (15)$$

Here,  $N_{sp}$  is the number of spheres and is equal to 1 for this case. The computed values are summarized in Table 1 for both approaches. The solutions converge to within about 2% of the analytic value,  $C_D = 2.810$  obtained by Zick & Homsy. We have also computed the apparent convergence rate,  $\mathcal{P}$  and the relative percent uncertainty using the GCI method. For this low Reynolds number the body fitted approach, wherein the no-slip condition is directly enforced at the sphere surface, has a very rapid apparent rate of convergence,  $\mathcal{P} = 3.19$ , leading to very low uncertainty in  $C_D$  for the fine grid solution. The fictitious domain approach, which less precisely defines the surface via the sub-grid marker points, converges at a more modest rate of  $\mathcal{P} = 1.65$ , and achieves a relative uncertainty of 0.59% for  $D/\Delta = 48$ . The roughly 4% discrepancy between the converged body fitted and fictitious domain solutions may be due to differences in grid quality (body fitted) and interface representation (fictitious domain)

Table 1: Comparison of Stokes flow drag coefficient to analytic solution of Zick and Homsy (1982) for a simple cubic array with solid concentration,  $(1 - \epsilon) = 0.064$

$D/\Delta$	Analytic	Body Fitted			Fictitious Domain		
	$C_D$	$C_D$	$\mathcal{P}$	GCI (%)	$C_D$	$\mathcal{P}$	GCI (%)
12	2.810	2.784	-	-	3.086	-	-
24	2.810	2.857	-	-	2.831	-	-
48	2.810	2.865	3.19	0.016%	2.750	1.65	0.59%

### 3.3. Effect of the contact point: The contacting pair

Inertial flow past a contacting pair of spheres in a confined channel is considered to study the effects of sphere to sphere contact regions on the flow **and to compare the hydrodynamic**

force measured by the two interface representations. The configuration of the connected body is shown in Figure 5a. The spheres are located such that their contact point always lies at the origin,  $(X, Y, Z) = 0$ . Uniform flow enters from a square cross section,  $3.5D \times 3.5D$ , at  $Z = -5D$ . A convective outflow boundary is located downstream of the contact at  $Z = +5D$ . A no-slip condition is enforced on the channel walls. The spheres are rotated around the  $Y$  axis by the angle of incidence,  $\theta$ , so that the leading and trailing sphere centers have the coordinates

$$(X_l, Y_l, Z_l) = \left( 0, -\frac{D}{2} \sin(\theta), -\frac{D}{2} \cos(\theta) \right) \quad (16)$$

$$(X_t, Y_t, Z_t) = \left( 0, \frac{D}{2} \sin(\theta), \frac{D}{2} \cos(\theta) \right) \quad (17)$$

The value of  $\theta$  is varied from  $0^\circ$  to  $90^\circ$  in increments of  $15^\circ$  in order to fully sample the range of orientations found in randomly packed beds. The uniform inflow velocity is assigned so the Reynolds number, defined  $Re = U_{in}D/\nu$ , ranges from 50 to 175, in increments of 25.

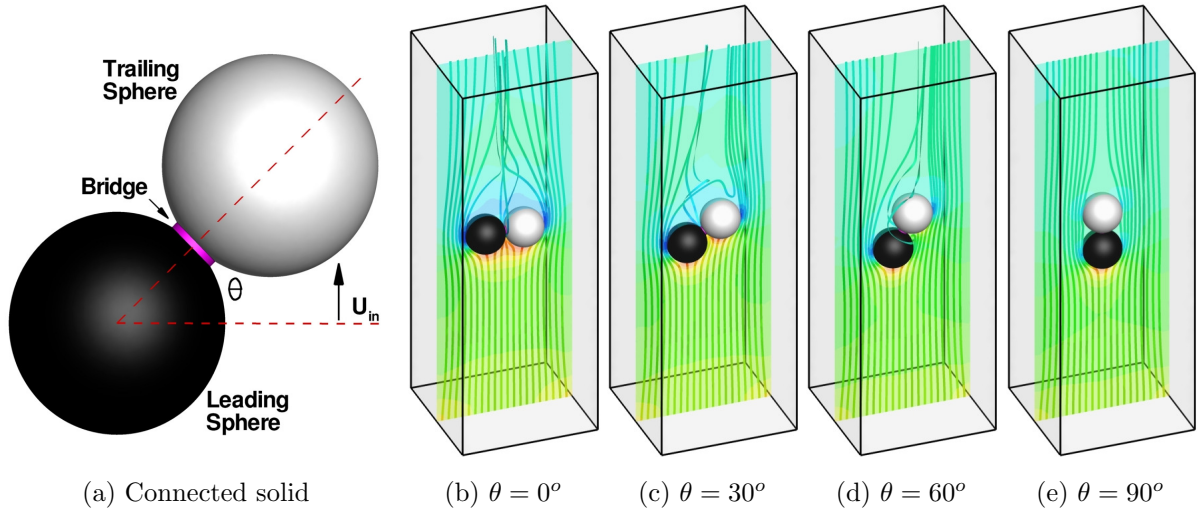


Figure 5: Configuration and flow visualization for the contacting pair case. (a) Shows the configuration of the connected body. (b-e) are stream ribbon visualization of flow around the pair of spheres at  $Re = 175$  and select angles of incidence. Pressure contours are shown in the  $X = 0$  plane; red indicates high pressure, blue indicates low pressure.

The flow is allowed to develop for  $tU_{in}/D = 30$  non-dimensional time units. To accelerate the development of the flow, solutions from consecutive Reynolds numbers are used as initial conditions (ie. the  $Re = 100$  solution is used as an I.C. for the  $Re = 125$  simulation). Mean grid spacing on the surface and in the vicinity of the pair is close to  $D/\Delta = 40$  for both approaches. The main purpose of this test case is to study the effect of the contact point on the near-sphere flow field, thus the grids are allowed to coarsen far away from the body. At a distance of  $1.5D$  away from the contact line, the grid spacing is never greater than twice the surface spacing. **To systematically compare the two methods, a grid sensitivity study of the  $Re = 175$  flow conditions is also discussed later on.**

We confirm that the flow has reached a steady state by monitoring the total drag force on the surface of the connected body. This is plotted in Figure 6 for  $(\theta, Re) = (0^\circ, 50)$  and  $(0^\circ, 175)$  along with similar results from Section 3.4, and demonstrates that 30 non dimensional time units is sufficient to achieve a steady, developed flow condition. Although the flow is steady, the fluid trajectories near the two spheres are quite complex at these Reynolds numbers. Figure 5b-e shows select stream-ribbons for  $\theta = 0^\circ, 30^\circ, 60^\circ,$  and  $\theta = 90^\circ$  along with pressure contours in the  $X = 0$  plane. At  $\theta = 0^\circ$ , the flow stagnates evenly on both spheres and the contact point, generating a large symmetric recirculation bubble. As the angle of incidence is increased to  $30^\circ$  and  $60^\circ$ , the recirculation bubble bends away from the leading sphere and towards the trailing sphere and the flow is no longer symmetric about the contact line. At  $\theta = 60^\circ$  there is a noticeable decrease in stagnation pressure on the trailing sphere, suggesting a drafting effect is present. At  $\theta = 90^\circ$ , symmetry is regained as the body becomes streamlined, and the contact point is completely obstructed from the oncoming flow by the leading sphere.

Using the body fitted approach, it is possible to isolate the streamwise drag force on the leading sphere,  $f_z^l$ , the trailing sphere,  $f_z^t$ , and the bridge,  $f_z^b$ , by directly computing the surface integral of viscous and pressure forces on each of these solid boundary zones. These measurements can be used to determine the relative contribution of the bridge region to the total drag of the connected body. In Figure 7 the ratio of drag force on the trailing and leading spheres ( $f_z^t/f_z^l$ ), as well as the ratio of drag force on the bridge to the leading sphere

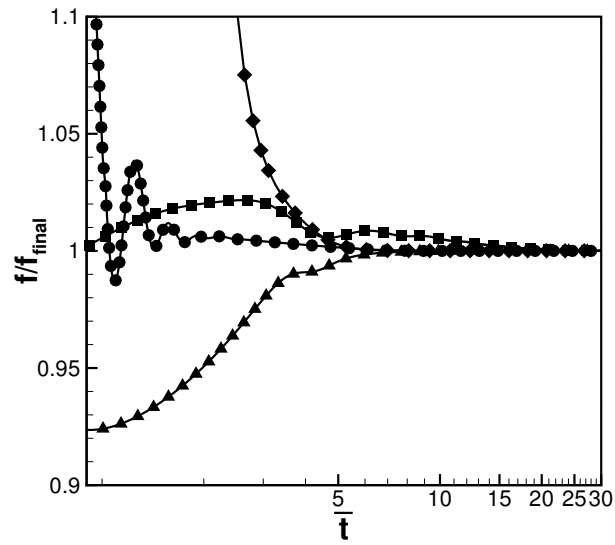


Figure 6: Semi-logarithmic plot of the time history of hydrodynamic force exerted on the spherical bodies for steady flow conditions in the contacting pair and simple cubic lattice test cases. The force in each case is normalized by the force at  $tU/D = 30$ . **▲** contacting pair at  $\theta = 0^\circ$ ,  $Re = 50$ , **■** contacting pair at  $\theta = 0^\circ$ ,  $Re = 175$ , **●** simple cubic lattice at  $Re = 12$ , **◆** simple cubic lattice at  $Re = 204$ .

$(f_z^b/f_z^l)$ , is plotted as a function of  $Re$  for each value of  $\theta$ . The first ratio demonstrates the increased drafting ability of the trailing sphere at increased  $\theta$  or increased  $Re$  as would be expected. The second ratio demonstrates that for all combinations of  $Re$  and  $\theta$ , the contribution of the bridge to the total drag of the pair is less than 1% of the leading sphere's contribution. This ratio is maximized at all  $Re$  for  $\theta = 0^\circ$ , and decreases as the bridge surface is rotated out of the stagnation region. Extrapolating the trend, the cylinder bridge drag will be 1% of the leading sphere drag at  $\theta = 0^\circ$  for  $Re \approx 600$ , the largest Reynolds number considered in this study.

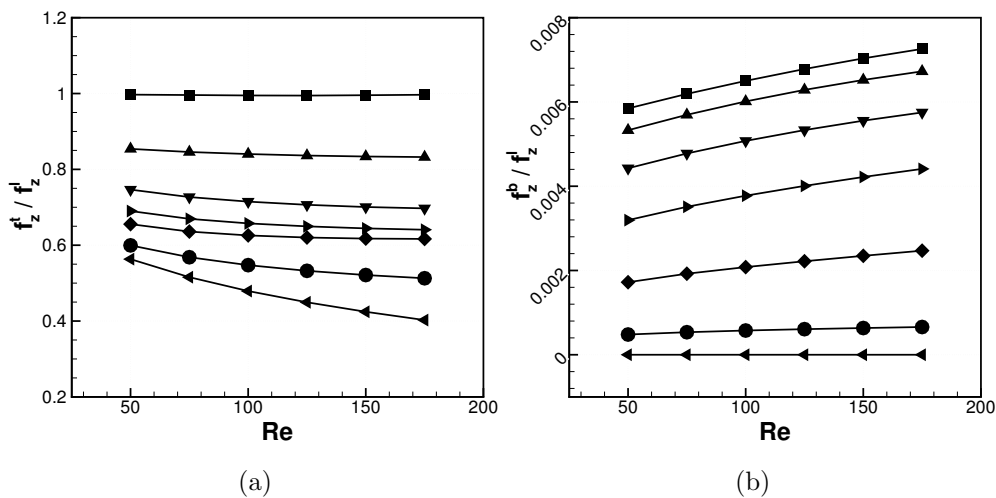


Figure 7: Drag force on portions of the connected body relative to the leading sphere drag as a function of  $Re$  for all values of  $\theta$  tested. (a) The trailing sphere drag,  $f_z^t/f_z^l$ . (b) The bridge drag,  $f_z^b/f_z^l$ .  $\blacksquare$   $\theta = 0^\circ$ ,  $\blacktriangle$   $\theta = 15^\circ$ ,  $\blacktriangledown$   $\theta = 30^\circ$ ,  $\blacktriangleright$   $\theta = 45^\circ$ ,  $\blacklozenge$   $\theta = 60^\circ$ ,  $\bullet$   $\theta = 75^\circ$ ,  $\blacktriangleleft$   $\theta = 90^\circ$ .

The hydrodynamic drag in the fictitious domain results is accessed through the net rigidity constraint force, and used to make direct comparisons with the body fitted solutions. For the  $Re = 175$  cases, a grid convergence analysis has been performed using three grid spacings for each method. In figure 8 the drag coefficient computed according to Equation 15<sup>1</sup> is plotted as a function of  $\theta$ . Results are shown for body fitted grid resolutions of  $D/\Delta = 22, 39, 72$  and fictitious domain grid resolutions of  $D/\Delta = 15, 25, 40$ . In

<sup>1</sup>For this case,  $N_{sp} = 2$  and  $U_p \epsilon = U_{in}$  when computing  $C_D$

addition, the  $C_D$  values, apparent convergence rates, and the GCI uncertainty levels are reported in Table 2 for each value of  $\theta$ . The fictitious domain approach shows near second order convergence for all cases and roughly 2% uncertainty for the  $D/\Delta = 40$  grids. The body fitted approach shows a much slower convergence rate, less than first order, but still achieves roughly 8% uncertainty with a grid resolution of  $D/\Delta = 72$ . For each value of  $\theta$ , the two approaches appear to be converging to a very similar grid independent value of  $C_D$ . To show this, the 8% uncertainty band has been plotted as error bars on the fine grid body fitted solution (the 2% error bars for the fictitious domain solution have been omitted for clarity). By extrapolating the convergence trends in this way it can be seen that the body fitted and fictitious domain solutions should converge to similar values in the limit of infinite grid resolution. The relatively slow convergence rate of the body fitted solution is most likely due to the local grid quality around the body, especially near the contact region where non-uniform, skewed elements are difficult to eliminate. This case is not intended to establish grid resolution requirements for realistic packed beds, but rather to provide confidence that the interface representation of both methods is consistent.

As a final demonstration of the consistency between the two methods, the velocity profile in the near wake behind the cylinder bridge is plotted in Figure 9 for  $Re = 175$ ,  $\theta = 0^\circ$ . Despite the close proximity of the probes to the solid boundaries, the wake profiles predicted by each approach are in very good agreement. These results demonstrate that the inability of both methods to completely resolve the contact point between two spheres should not significantly affect global or local flow properties in packed beds.

#### *3.4. Performance in porous geometries: Flow through a simple cubic lattice*

In this test case, pore scale flow through square channels filled with a simple cubic lattice of spheres is examined. The configurations are chosen to be similar to the experiments of Suekane et al. (2003) who used MRI techniques to make detailed three dimensional measurements of the porescale velocity field. To our knowledge, it is one of the only experimental measurements of its kind, and has served as a validation for several other numerical studies including Gunjal et al. (2005) and Ovaysi and Piri (2010). We consider two slightly different

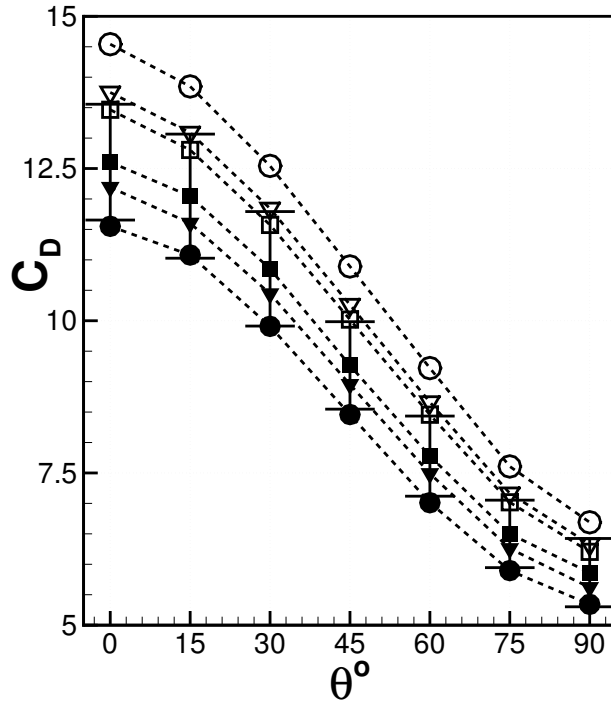


Figure 8: Grid convergence of  $C_D$  for the contacting pair at  $Re = 175$ , and all angles of incidence. Body fitted solution:  $\bullet$   $D/\Delta = 22$ ,  $\blacktriangledown$   $D/\Delta = 39$ ,  $\blacksquare$   $D/\Delta = 72$ . Fictitious domain solution:  $\circ$   $D/\Delta = 15$ ,  $\nabla$   $D/\Delta = 25$ ,  $\square$   $D/\Delta = 40$

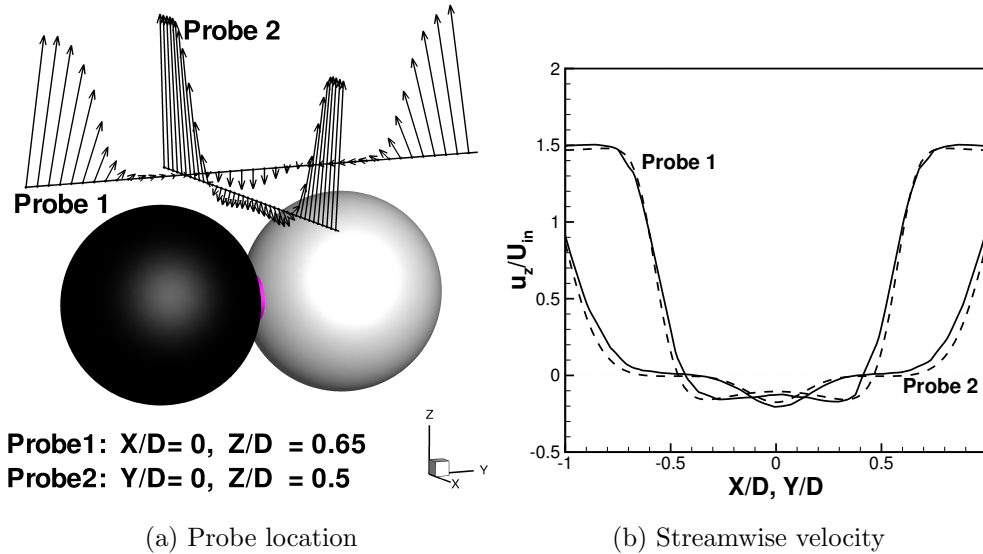


Figure 9: Velocity profiles in the near wake behind the contacting pair at  $Re = 175$ ,  $\theta = 0^\circ$ . (a) Probe locations. (b) Streamwise velocity profile (—)body fitted, (- - -)fictitious domain.

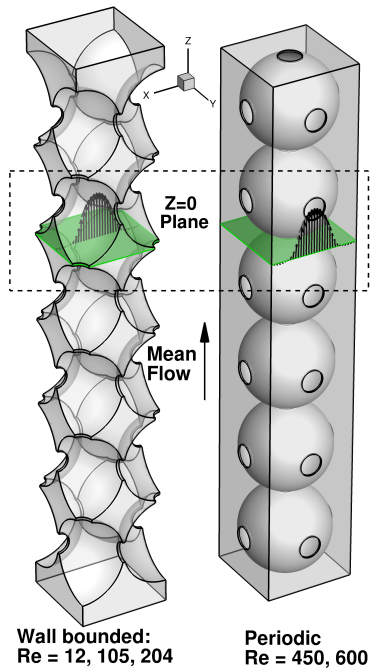
Table 2: Grid convergence of  $C_D$  for the contacting pair at  $Re = 175$ , and all angles of incidence

$\theta$	Body Fitted				Fictitious Domain			
	$D/\Delta$	$C_D$	$\mathcal{P}$	GCI(%)	$D/\Delta$	$C_D$	$\mathcal{P}$	GCI (%)
$0^\circ$	22	11.6	-	-	15	14.5	-	-
	39	12.2	-	-	25	13.8	-	-
	72	12.6	0.84	7.55%	40	13.5	1.90	1.89%
$15^\circ$	22	11.1	-	-	15	13.8	-	-
	39	11.6	-	-	25	13.1	-	-
	72	12.0	0.39	8.46%	40	12.8	1.81	1.99%
$30^\circ$	22	9.91	-	-	15	12.5	-	-
	39	10.4	-	-	25	11.8	-	-
	72	10.9	0.55	8.67%	40	11.6	1.77	2.08%
$45^\circ$	22	8.46	-	-	15	10.9	-	-
	39	8.95	-	-	25	10.3	-	-
	72	9.27	0.88	7.75%	40	10.0	1.75	2.17%
$60^\circ$	22	7.01	-	-	15	9.22	-	-
	39	7.49	-	-	25	8.66	-	-
	72	7.77	0.97	8.46%	40	8.46	1.85	2.18%
$75^\circ$	22	5.90	-	-	15	7.61	-	-
	39	6.26	-	-	25	7.16	-	-
	72	6.50	0.79	8.53%	40	7.02	2.07	1.86%
$90^\circ$	22	5.34	-	-	15	6.69	-	-
	39	5.62	-	-	25	6.33	-	-
	72	5.86	0.32	9.57%	40	6.20	1.97	1.80%

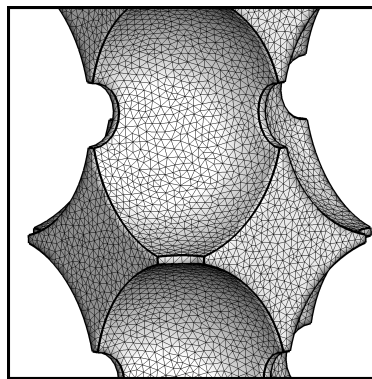
computational domains shown in Figure 10a. The first configuration, intended to match the experiments of Suekane et al. (2003) as closely as possible, consists of six layers of diameter  $D = 28mm$  quarter spheres located in the corners of the channel, with no-slip boundaries enforced on the exterior channel walls. This domain is used to simulate Reynolds numbers based on the pore velocity,  $U_p$ , of  $Re = U_p D / \nu = 12.17, 105.57, \text{ and } 204.74$ , allowing for direct comparison with the experiments. Flow in this configuration is driven by a constant inflow boundary, located  $5D$  upstream of the first sphere (not shown in the Figure), where  $U_{in} = \epsilon U_p$ , and the fluid fraction is  $\epsilon = 0.476$  for this arrangement. A convective outlet is located  $5D$  downstream of the last sphere. The flow is started from rest and simulated for  $tU_p/D = 10$  non dimensional time units for each Reynolds number, which is sufficient to obtain a fully developed steady flow field as confirmed in Figure 6.

In order to test the performance of the solvers for unsteady flows with vortex shedding, a second configuration is considered to simulate  $Re = 450$  and  $600$  as there is no experimental data in this flow regime. This configuration consists of six layers of complete spheres stacked in the center of the channel. It has periodic boundaries on all exterior channel walls which allows for faster symmetry breaking and transition to unsteady flow. The flow is initialized with large wavelength sinusoidal fluctuations and the flow is simulated for at least  $tU_p/D = 60$  time units to allow the unsteady dynamics to reach a stationary state. During the simulation, a body force is continuously adjusted so that the target Reynolds numbers are achieved. At the end of all simulations, the flow is probed along the line  $Y = 0, Z = 0$ , as shown in Figure 10a, which traverses the center of the fifth pore in both configurations.

For the body fitted approach, the domains are discretized using unstructured, tetrahedral meshes as described earlier. Each full or quarter sphere was created at its exact diameter inside the channel. Then a small cylindrical region of fluid, with diameter  $D_b = 0.25D$ , is removed from the near the contact points. The entire connected solid is subtracted from the channel resulting in a watertight solid boundary. Uniform size tetrahedral elements with  $\Delta \approx \mathcal{V}_{cv}^{1/3}$  are created throughout the channel. A closeup view of the surface of the body fitted mesh with  $D/\Delta = 64$  is shown in Figure 10b. The tetrahedral grids are high quality; the maximum cell aspect ratio is 4 or less for all meshes. Regular Cartesian grids are used for



(a) Computational Domains



(b) Surface Mesh

Figure 10: Setup of flow through a simple cubic lattice. (a) shows the two computational domains used. The orientation of the line probe used is indicated by the vector velocity profiles. (b) shows the  $D/\Delta = 64$  surface mesh used in the body fitted simulations.

Table 3: Grids used to simulate flow through the simple cubic lattice.

	$D/\Delta = 128$		$D/\Delta = 64$		$D/\Delta = 32$		$D/\Delta = 16$	
	Tet.	Cart.	Tet.	Cart.	Tet.	Cart.	Tet.	Cart.
$N_{cv}$ Inflow/Outflow	7.62M	17.9M	1.13M	2.245M	190k	281k	54k	35k
$N_{cv}$ Periodic	6.33M	12.6M	867k	1.57M	119k	196k	n/a	n/a

the fictitious domain approach which include both the fluid and solid portions of the channel. Four meshes were generated for each method with mean spacing,  $D/\Delta = 16, 32, 64, 128$ . The total cell count for each mesh is summarized in table 3.

Fine, medium, and coarse grid results are used to estimate the uncertainty in the fine grid solution obtained with each approach by applying the *GCI* method outlined in Section 2.3. For  $Re = 12$ , grids with  $D/\Delta = 64, 32$ , and  $16$  are used, while the  $Re = 105, 204, 450$ , and  $600$  simulations use grids with  $D/\Delta = 128, 64$ , and  $32$ . Since grid independence of one flow property does not necessarily imply grid independence of another, it is important to use multiple measures to fully understand the convergence behavior. For the steady flow rates, the grid convergence properties are computed for the streamwise velocity component,  $\phi = u_z$ , as well as the non-dimensional macroscale pressure gradient,  $\phi = \Psi = \frac{\Delta P}{L} \frac{D}{\rho U_p^2} \frac{\epsilon}{1-\epsilon}$ . For  $\phi = u_z$  we are directly assessing the convergence of the porescale velocity field, while for  $\phi = \Psi$ , we are assessing the convergence of a macroscale integrated property. For the unsteady flow rates, the analysis is done for the time averaged streamwise velocity,  $\phi = \overline{u_z}$ , as well as the time averaged turbulent kinetic energy,  $\overline{TKE} = \overline{\sum u_i'^2}$ . These two measures capture the mean and fluctuating character of the porescale flow respectively. Key results of the analysis are reported in table 4. For all porescale properties the max and RMS value of  $\phi$  predicted by the two approaches are in reasonably good agreement, with the exceptions discussed further below. The monotone convergence rate is significantly higher for the fictitious domain approach in all cases, indicating that the solutions on the three Cartesian grids are more fully in the asymptotic regime relative to the body fitted tetrahedral grid results. The global apparent rate of convergence,  $\mathcal{P}_G$ , is bound by the formal second order

Table 4: Grid convergence results for flow through the simple cubic lattice. In all cases  $D/\Delta_1$ ,  $D/\Delta_2$ ,  $D/\Delta_3 = 128, 64, 32$  except  $Re = 12.12$  where  $D/\Delta_1$ ,  $D/\Delta_2$ ,  $D/\Delta_3 = 64, 32, 16$ . Values are reported in  $mm/s$  for velocity, and  $mm^2/s^2$  for  $TKE$ .

$Re$	$\phi$	$MAX(\phi)$		$RMS(\phi)$		$M_n[\%]$		$\mathcal{P}_G$		$GCI_G[\%]$		$D/\Delta_{5\%}$	
		BF	FD	BF	FD	BF	FD	BF	FD	BF	FD	BF	FD
12	$u_z$	1.98	1.71	0.53	0.50	62	95	1.73	1.35	3.61	1.60	53	28
12	$\Psi$	n/a	n/a	13.9	13.4	n/a	n/a	1.43	1.67	2.94	3.69	44	53
105	$u_z$	16.0	15.9	4.61	4.53	65	82	1.76	1.65	1.89	0.54	74	33
105	$\Psi$	n/a	n/a	2.17	2.18	n/a	n/a	2.72	1.30	0.10	1.98	30	62
204	$u_z$	30.7	30.9	8.99	8.85	66	88	1.82	1.62	1.99	0.90	77	44
204	$\Psi$	n/a	n/a	1.29	1.33	n/a	n/a	3.34	1.41	0.03	2.91	28	87
450	$\overline{u_z}$	61.4	56.2	24.2	24.2	41	84	1.84	1.56	4.77	2.20	125	76
450	$\overline{TKE}$	230	284	64.8	82.8	52	66	1.76	1.71	16.1	3.93	249	111
600	$\overline{u_z}$	75.5	72.3	32.1	32.1	47	80	2.08	1.29	2.75	3.79	96	103
600	$\overline{TKE}$	436	458	143	153	47	67	1.84	1.45	10.4	5.42	191	135

accuracy of the spatial discretization schemes (with a few exceptions discussed below), and is observed to be between roughly 1.3 and 2. In general, it is slightly higher for the body fitted results. Even though the convergence rate is higher, the difference between the fine and medium grid solutions ( $\phi_1 - \phi_2$ ) is in general much more significant with the body fitted approach, leading to a much higher global uncertainty,  $GCI_G$ , of the porescale quantities in most cases. The convergence of the integral pressure drop at the steady flow rates behaves differently and is discussed in more detail below. From the uncertainty estimates associated with the fine grid solutions, the grid density required to achieve a 5% uncertainty level,  $D/\Delta_{5\%}$  is estimated from equation 11. In many cases, the grid requirements based on the porescale quantities are significantly stricter for the the body fitted approach.

It is helpful to take stock of the results in the table in more detail while at the same time examining the grid convergence behavior graphically. The fine, medium, and coarse grid

predictions of streamwise velocity along the  $Y = 0$ ,  $Z = 0$  line are plotted in Figure 11a-c for the steady flow rates. In this Figure as well as Figures 13 and 15, the body fitted solutions are shown in the left hand column and the fictitious domain solutions are shown in the right hand column. In the main portion of the sub-figures, only the fine grid result with error bars corresponding to  $GCI(\mathbf{x})$  is plotted for clarity alongside the experimental data of Suekane et al. (2003). In the insets, the medium and coarse grid solutions are shown as well, for the region near  $|X/D| \lesssim 0.15$ , to illustrate the convergence with grid refinement. In both methods, refinement results in convergence of the solution towards the experimental data. The maximum and RMS values of  $u_z$  are similar for all cases on the fine grids. In all cases there is good agreement between the experimental data points, and the medium to fine grid solutions. It is evident that as Reynolds number is increased, the significant flow inertia gives rise to a strong jet through the center of the pore ( $|X/D| \lesssim 0.15$ ), and symmetric backflow regions close to the walls ( $|X/D| \approx 0.35$ ) for  $Re = 105$  and  $204$ . For these steady results, the global apparent rate of convergence,  $\mathcal{P}_G$ , is roughly 1.75 for the body fitted results and varies from 1.35 to 1.65 for the fictitious domain results. This overall lower rate of convergence may be due to the higher percentage of monotone nodes,  $\%M_n$ , obtained with the fictitious domain approach, 82% or more. Despite enjoying a slightly better convergence rate, the global relative uncertainty of the fine grid body fitted solution,  $GCI_G$ , is roughly two to three times more than the fictitious domain solution in each case. This indicates that local errors are introduced by the unstructured meshes, similar to the observations made in the Taylor vortex case. Using equation 11, the grid density required to obtain a (relatively arbitrary) target global uncertainty level of 5% was computed and found to be about twice as much for the body fitted approach. For this fixed level of uncertainty, these steady Reynolds numbers will require between 53 and 77  $cv/D$  with the body fitted tetrahedral grids, but only 28 to 44  $cv/D$  with a Cartesian grid and the fictitious domain approach.

The non dimensional pressure drop for the steady flow rates predicted by both methods using the fine grid is plotted in a Figure 12 alongside the correlation of Ergun (1952) for random packed beds. To produce the data points, the pressure is spatially averaged in two

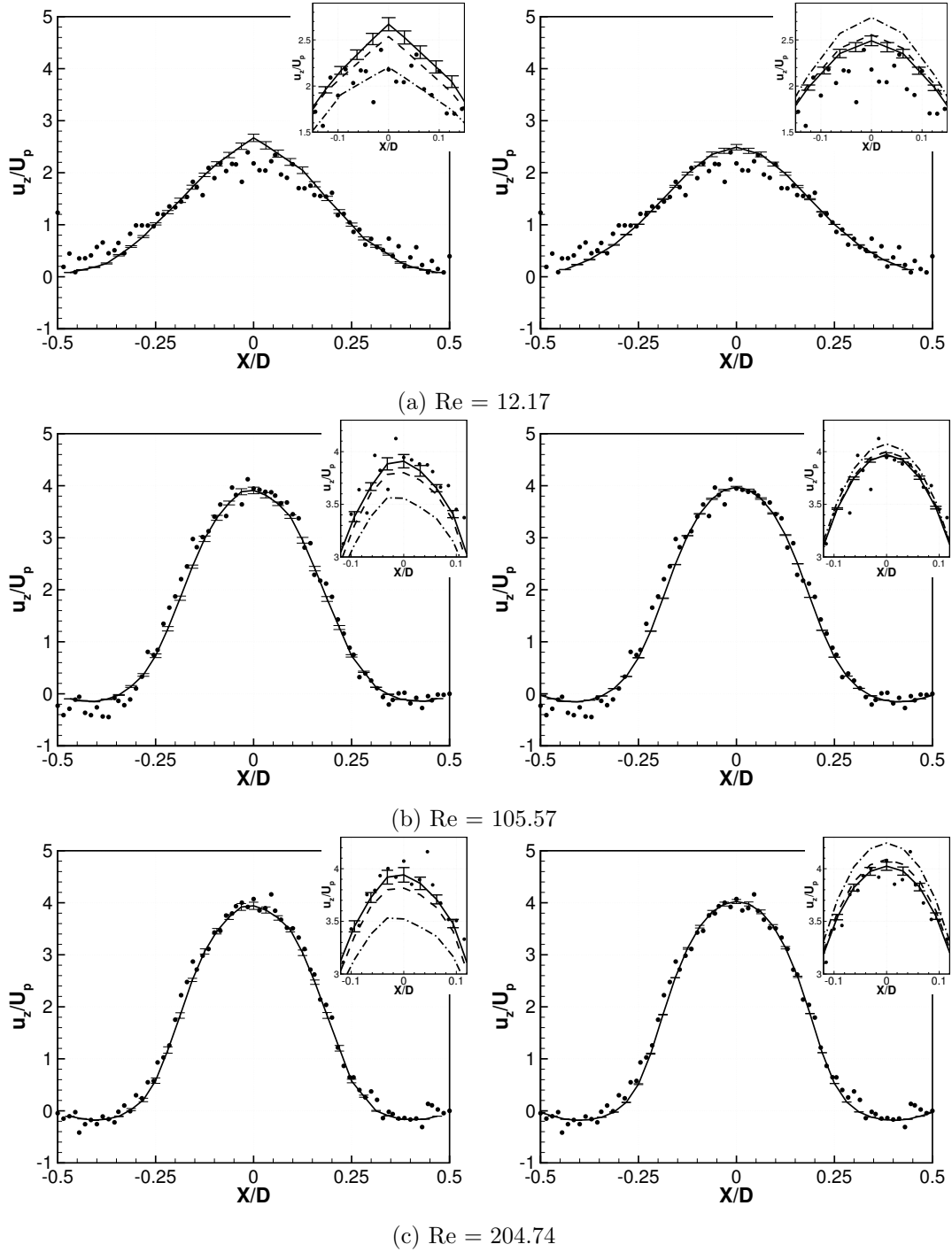


Figure 11: Comparison of interstitial velocity profiles with the data of Suekane et al. (2003) Along the  $Y = 0, Z = 0$  line probe shown in Figure 10a. (—) Fine Grid  $\Delta_1$  shown with error bars, (- - -) Medium Grid  $\Delta_2$ , (- · -) Coarse Grid  $\Delta_3$ , ● Experiment. Left column shows body fitted solution. Right column shows fictitious domain solution.

planes located  $L = 2D$  apart in the streamwise direction once the flow is fully developed. The figure and the results in table 4 show that the results from both types of simulations are in agreement in the fine grid solutions. However, the GCI analysis indicates that there is significantly less uncertainty in the body fitted result (especially for  $Re = 105$  and  $204$ ), which is surprising given the observations of the interstitial velocity profiles. Inspection of the convergence trends shows that the body fitted pressure drop converges at a rate higher than the formal second order of accuracy of the code. This raises questions about the reliability of using such a result, and shows the danger of using integral measurements alone to assess grid convergence of the pore scale flow field. Deviation of the results from the Ergun correlation at increased Reynolds numbers is most likely a result of the simple cubic arrangement, and has also been reported by Gunjal et al. (2005). This particular configuration allows a high inertia jet to develop in the center of the channel which is not typically seen in the large random configurations the correlation was developed from.

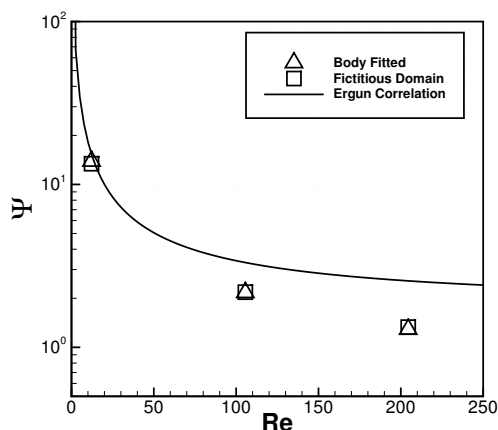
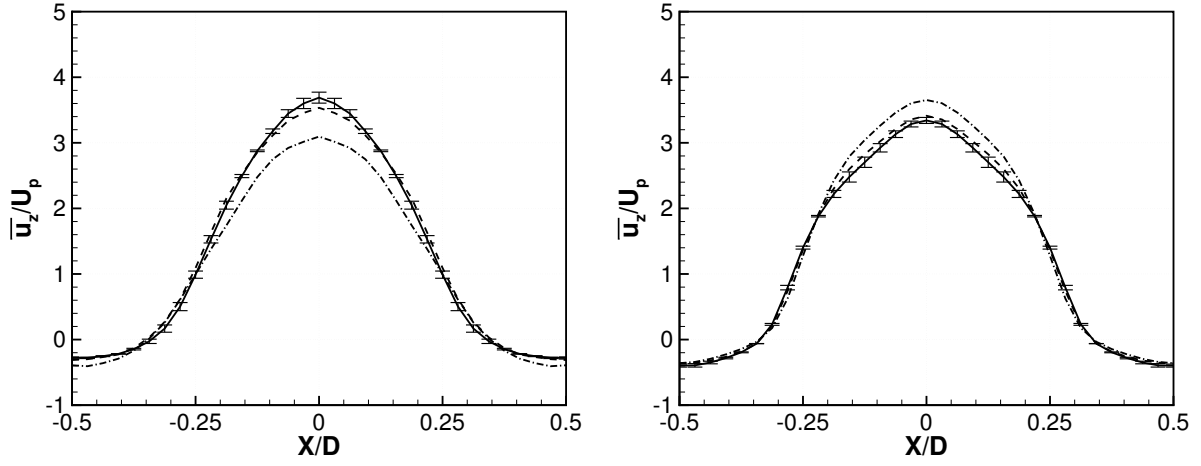
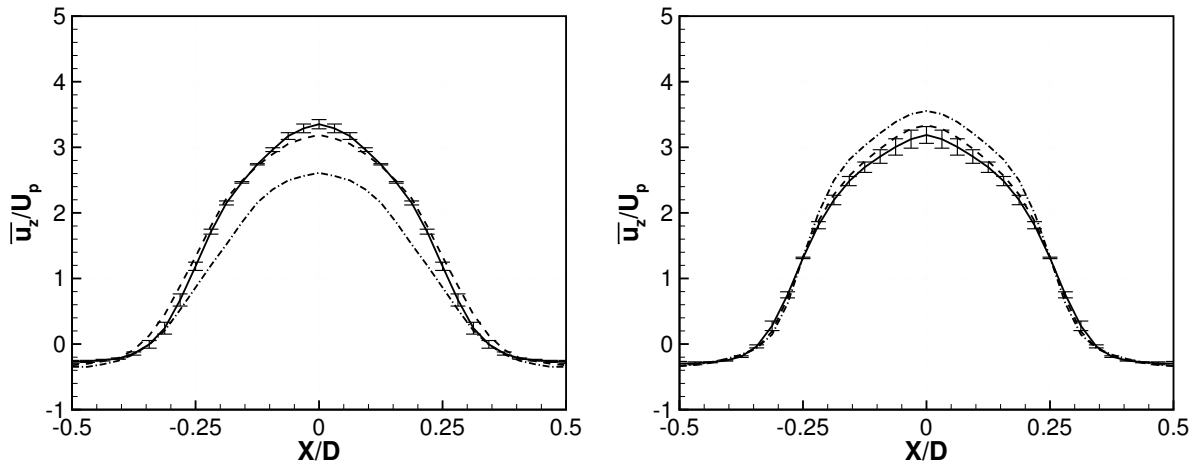


Figure 12: Non-dimensional pressure drop as a function of Reynolds number for steady flow through the simple cubic lattice.

We now consider results from the two unsteady Reynolds numbers in the periodic domain. In Figure 13, the interstitial profiles of the time averaged streamwise velocity  $\overline{u_z}$  are shown along the  $Y = 0, Z = 0$  line probe. The global relative uncertainty for the fine grid solution is good for both methods, less than 5% in each case. At  $Re = 600$  the fine grid mean velocity profiles (Figure 13b) are in good agreement. Examination of the interstitial



(a)  $Re = 450$



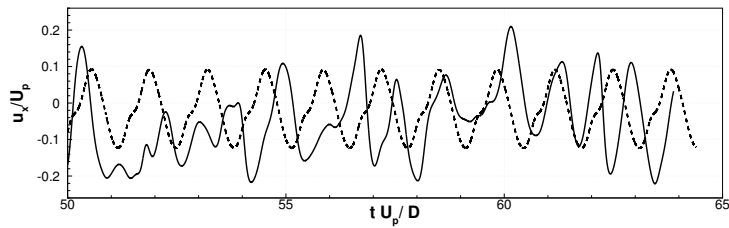
(b)  $Re = 600$

Figure 13: Time averaged streamwise velocity component along the line  $Y/D = 0$ ,  $Z/D = 0$  for unsteady flows in the periodic simple cubic lattice. Left column shows body fitted solution. Right column shows fictitious domain solution. (—) Fine Grid  $\Delta_1$  shown with error bars, (- - -) Medium Grid  $\Delta_2$ , (- · -) Coarse Grid  $\Delta_3$ .

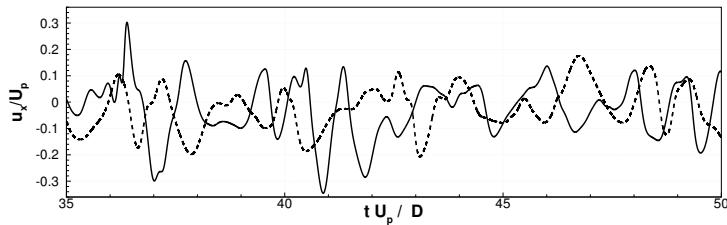
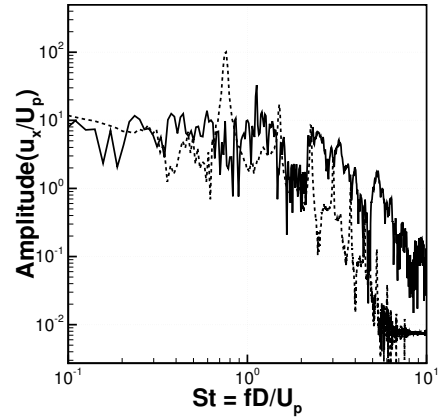
velocity profiles at  $Re = 450$  (Figure 13a), however, reveals a noticeable discrepancy between the body fitted and fictitious domain predictions. In the fictitious domain solution, the average velocity profile is flattened out somewhat in the pore center, while the body fitted profile retains a larger maximum velocity and the parabolic character observed at  $Re=105$  and  $204$ . This suggests that the porescale unsteady dynamics predicted by the two approaches may be different. This suspicion is confirmed by Figure 14, which shows the time history and frequency spectra of the transverse ( $X$ ) velocity component at the point  $X/D = -0.36$ ,  $Y/D = 0$ ,  $Z/D = 0$  computed on the fine grid using both approaches. At  $Re = 450$ , a single dominant frequency with a Strouhal number of  $St = fD/U_p \approx 0.75$  is evident in the body fitted solution, while the fictitious domain solution shows energetic fluctuations over a broader range of frequencies. Interestingly, the fluctuations observed by both methods at  $Re = 600$  seem to be in better agreement. The transition to unsteadiness and turbulence in packed beds is a very sensitive process, and it is possible that the dynamics of weakly unsteady flows could be altered by the type of grid being used. Tetrahedral grids cells will, in general, be more susceptible to numerical diffusion than uniform hexahedral cells. We believe that especially for flows in this transitional (sub turbulent) regime, modest amounts of dissipation due to the grid type could lead to noticeable changes in the dynamics of the mean flow.

A more appropriate level of confidence for these Reynolds numbers can be obtained by examining the uncertainty in the  $\overline{TKE}$  distribution, shown in Figure 15. The fictitious domain approach has relatively low global uncertainty of around 4-5% on the fine grid and the main features seem to be captured along the interstitial profiles, even on coarse grids. The body fitted approach on the other hand has much larger global uncertainty, 16% and 10% for  $Re = 450$  and  $600$  respectively, and the peaks in the interstitial profile change significantly on the coarse, medium and fine grids. At  $Re = 450$ , both the mean and RMS values of TKE are significantly lower in the body fitted solution relative to the fictitious domain solution, indicating more dissipation may be occurring due to the unstructured meshes.

These unsteady flow results underscore a troubling aspect of uncertainty assessment



(a)  $Re = 450$



(b)  $Re = 600$

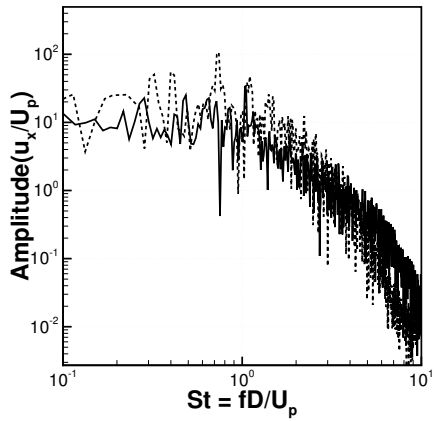
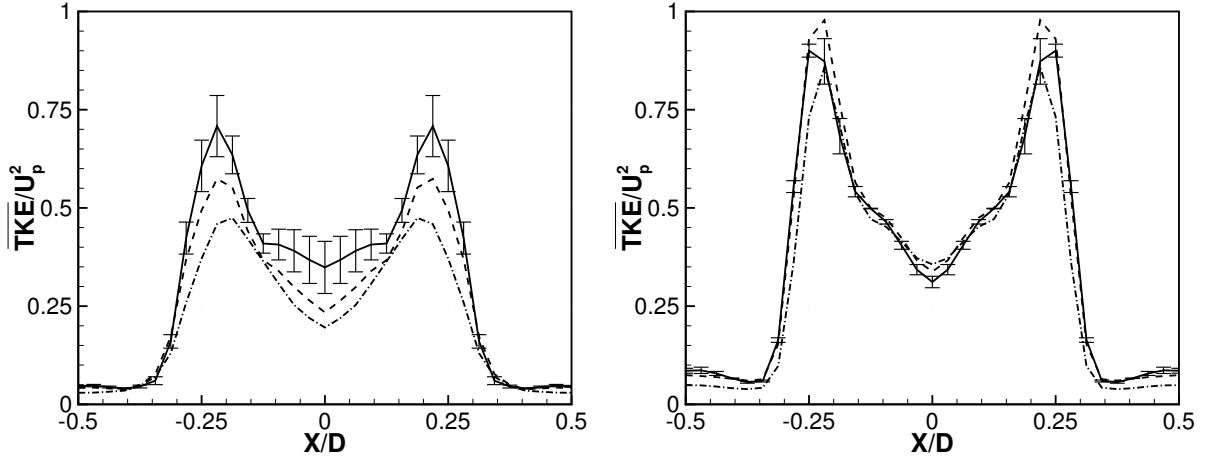
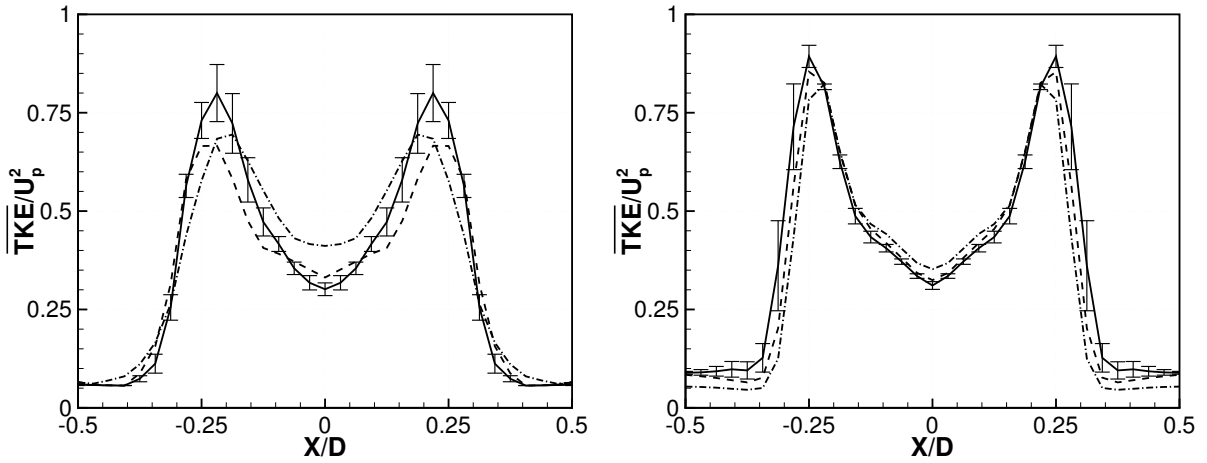


Figure 14: Time history of the transverse velocity component,  $u_x$ , and its non-dimensional frequency spectra at a point in the main recirculation zone ( $X/D = -0.36$ ,  $Y/D = 0$ ,  $Z/D = 0$ ) for the two unsteady Reynolds numbers simulated. (---) Body fitted approach, (—) fictitious domain approach.



(a)  $Re = 450$



(b)  $Re = 600$

Figure 15: Time averaged turbulent kinetic energy along the line  $Y/D = 0$ ,  $Z/D = 0$  for unsteady flows through the simple cubic lattice. Left column shows body fitted solution. Right column shows fictitious domain solution. (—) Fine Grid  $\Delta_1$  shown with error bars, (- - -) Medium Grid  $\Delta_2$ , (- · -) Coarse Grid  $\Delta_3$ .

for CFD results in general. Quantities of interest in numerical solutions to complex flow problems need not converge in the same way, and false positives may indicate convergence in one variable when another is unresolved. In our case we may very reasonably judge that when using the body fitted approach the medium grid should provide a high quality solution for  $Re = 450$  if we only consider convergence of the mean flow, when in fact the unsteady velocity fluctuations are unresolved and appear to degrade the accuracy of the time averaged solution. This emphasizes the need for thorough and quantitative grid convergence studies in CFD, especially for the complex configurations presented by packed bed and porous media flows.

#### 4. Scale up to realistic packed bed simulations

With the results presented up to this point in mind, it is possible to estimate the computational expense required for simulation of more general packed bed problems. Consider a rigid container which contains a matrix of randomly arranged spheres. The volume of the computational domain which must be meshed can be written in terms of the sphere diameter,  $D$ , as  $\mathcal{V}_c = \epsilon_m N_c D^3$ , where  $N_c$  relates the container volume to the sphere diameter (ie. a  $3D \times 3D \times 6D$  container has  $N_c = 54$ ), and  $\epsilon_m$  is the *effective meshing porosity*. It is equal to 1 in the fictitious domain approach, where the entire fluid/solid region is meshed, and equal to  $\epsilon$  in the body fitted approach where only the fluid domain must be discretized. For  $\Delta = \mathcal{V}_{cv}^{1/3}$ , the total number of control volumes,  $N_{cv}$ , required to mesh the volume,  $\mathcal{V}_c$ , will be:

$$N_{cv} = \epsilon_m N_c \left( \frac{D}{\Delta} \right)^3 \quad (18)$$

For the time accurate solutions obtained in this work, the time step,  $\Delta_t$ , is restricted for temporal accuracy by the *CFL* number, which we define following Kim and Choi (2000) for an arbitrary cell as,

$$CFL = \frac{1}{2} \frac{1}{\mathcal{V}_{cv}} \sum_{faces} |U_f A_f| \Delta_t \quad (19)$$

Where  $A_f$  is the area of a single cell's face. If we assume that the length  $A_f/\mathcal{V}_{cv}$  is constant for all faces of a given cell (true for all regular polyhedra), and we assume the face velocity to be proportional to the pore velocity, we can re-write the  $CFL$  number as,

$$CFL = \frac{\mathcal{C}_s |U_p| \Delta_t}{\Delta} \quad (20)$$

Where cell shape factor,  $\mathcal{C}_s = \frac{A_{fa}}{\mathcal{V}_{cv}^{2/3}}$ , has been introduced. This ratio of areas is equal to 1 for cubic cells, and 1.81 for *perfect* (regular) tetrahedral cells. In practice, it is difficult to mesh a complex three dimensional domain with perfect tetrahedral cells everywhere and  $\mathcal{C}_s$  can be much higher. On average for our tetrahedral meshes, we see that the time step must be 5 times lower when compared to the Cartesian mesh of the same resolution to obtain the same  $CFL$ , implying that  $\mathcal{C}_s \approx 5$ . With this in mind, we can express the total number of timesteps,  $N_t$ , required to simulate one non-dimensional time unit,  $t = \frac{D}{U_p}$ , as

$$N_t = \frac{t}{\Delta_t} = \frac{\mathcal{C}_s}{CFL} \cdot \frac{D}{\Delta} \quad (21)$$

For perfect parallel scalability the computational expense (CPU-Hrs), of a time accurate, finite volume simulation is proportional to  $N_{cv}$  times  $N_t$ , implying that,

$$CPU \propto (\epsilon_m N_c) \cdot \left( \frac{\mathcal{C}_s}{CFL} \right) \cdot \left( \frac{D}{\Delta} \right)^4 \quad (22)$$

The present finite volume solver shows good (nearly perfect) scalability for up to 500 processors (Ham et al., 2003). The constant of proportionality in equation 22 could in general be dependent on  $Re$ ,  $CFL$ ,  $D/\Delta$ , as well as the hardware being used to run the simulation, and is difficult to measure. Nonetheless, it is important to note that the computational expense should scale like  $\left(\frac{D}{\Delta}\right)^4$ . The speedup which is obtainable by moving from a body fitted to fictitious domain simulation of flow through a packed bed can be estimated from the GCI analysis presented in Section 3.4. If we require a fixed level of uncertainty in our solution variable,  $\phi$ , say 5%, we can set the grid resolution,  $D/\Delta$ , in equation 22 to the required grid resolutions from table 4. We find that the theoretical speedup factor,  $\mathcal{S} = CPU_{BF}/CPU_{FD}$ , listed in table 5 for each case is between 1.9 and 65.

These estimates may seem unreasonably large until investigating actual CPU timings in as close of a 1:1 comparison as possible, for example, flow through the periodic simple

Table 5: Estimated simulation speedup for obtaining a solution with 5% uncertainty.  $\mathcal{S} = CPU_{BF}/CPU_{FD}$  computed using equation 22.

$Re$	$\phi$	$D/\Delta_{5\%}$		$\mathcal{S}$
		BF	FD	
12	$u_z$	53	28	36
105	$u_z$	74	33	63
204	$u_z$	77	44	24
450	$\overline{u_z}$	125	76	19
450	$\overline{TKE}$	249	111	65
600	$\overline{u_z}$	96	103	1.9
600	$\overline{TKE}$	191	135	10

cubic lattice. For this case, the CPU times required to simulate one non-dimensional time unit are summarized in table 6. This case was run with both methods at  $Re = 450$  and 600 using  $CFL \approx 0.5$ . Simulations using the  $D/\Delta = 64$  and 128 grids were performed on the Lonestar supercomputer at the Texas advanced supercomputing center. For the same  $Re$  and  $D/\Delta$ , the fictitious domain simulation requires significantly less CPU time, between 63% and 84% as much as the body fitted simulation. The GCI analysis of the results has shown that if less than 5% uncertainty is required in the solution, the body fitted simulation could require double the grid density of the fictitious domain simulation. Combining these two observations suggests that an actual speedup of about 5 times is likely for solutions of equivalent uncertainty. In practice the desired uncertainty level may be more or less strict than the 5% level used for the estimates here, leading to higher or lower grid density requirements. However, these scalability and speedup estimates should retain about the same character.

## 5. Flow through a randomly packed bed

Table 6: Observed computational expense using both approaches for simulating the Suekane case in a periodic domain with  $CFL \approx 0.5$

$D/\Delta$	$Re$	CPU-Hr/( $D/U$ )	
		Body Fitted	Fictitious Domain
64	450	111	80
128	450	340	284
64	600	118	87
128	600	470	298

We now examine the case of flow through a random sphere pack using the fictitious domain approach. This is intended to demonstrate the capability of the fictitious domain approach for the random sphere arrangements typical of engineering applications. The packing we consider is a relatively loose arrangement of 51 spheres in a box with sides  $L_x = L_y = L_z = 4D$ , resulting in the void fraction  $\epsilon = 0.58$ . It was generated using a *ballistic deposition* algorithm, similar to the method employed by Atmakidis and Kenig (2009). The flow is driven in the positive  $Z$  direction by a constant inflow velocity boundary located  $3D$  upstream of the packing so that the Reynolds number for the flow is  $Re = \frac{U_p * D}{\nu} = 600$ , where  $U_{in} = U_p \epsilon$  is the assigned inflow velocity. A convective outlet condition is located  $3D$  downstream of the packing. The flow is started from rest and allowed to develop to a non-dimensional time  $tU_p/D = 130$ .

The fictitious domain approach was chosen for this case because of the superior scalability demonstrated in the previous section as well as the guarantee of good mesh quality, even for random packings. Three Cartesian grids with uniform spacing  $\Delta = D/80, D/56, D/40$  in the porespace are used to quantify the grid convergence. The grids are stretched toward the inlet and outlet faces so that the grids contain a total of 47 million, 16 million and 5 million control volumes, respectively. These grids provide a roughly constant refinement ratio of  $r_{21} \approx r_{32} = 1.4$ .

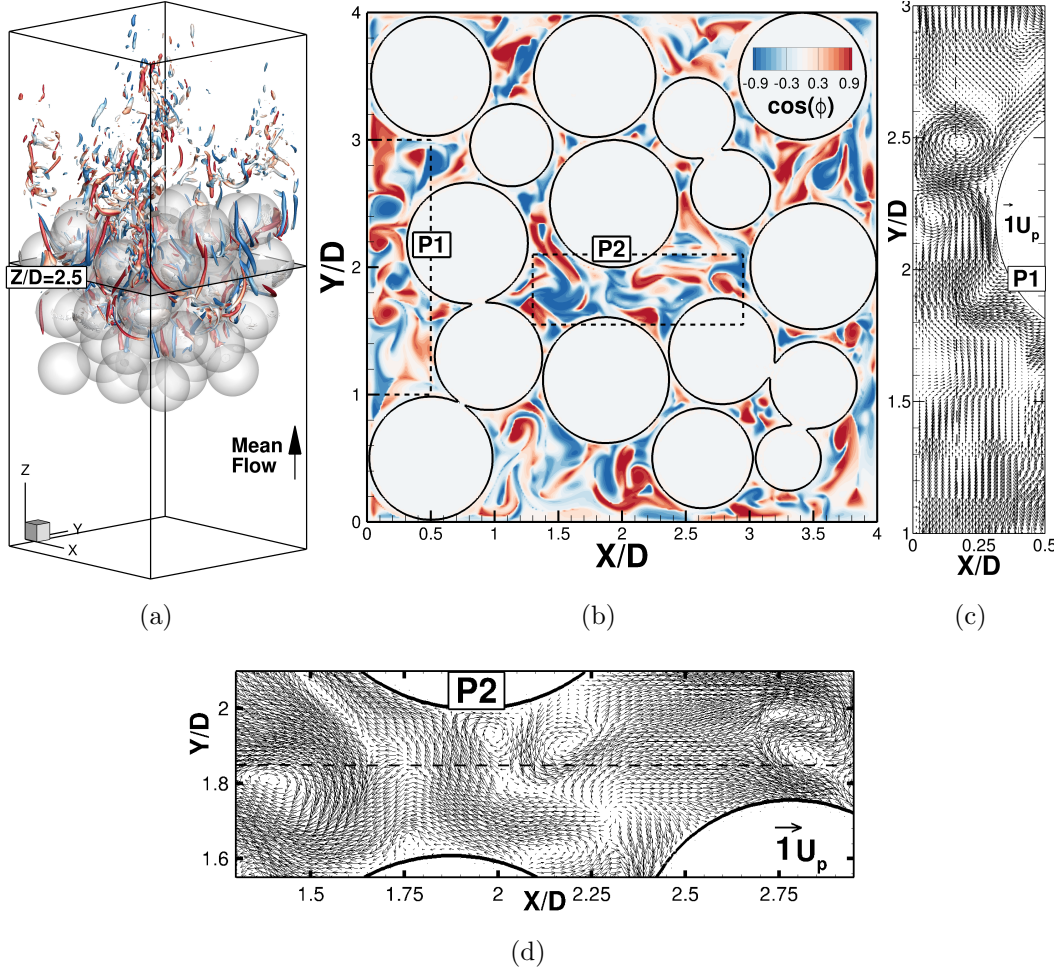


Figure 16: Visualization of the instantaneous porescale flow through the randomly packed bed of  $N_{sp} = 51$  spheres. (a) shows the simulation domain and sphere surfaces (transparent) along with instantaneous vortical structures corresponding to isosurfaces of  $\lambda_{ci}/\lambda_{ci}^{max} = 0.25$ . The isosurfaces are colored by  $\cos(\phi)$ , indicating relative helicity. (b) shows contours of  $\cos(\phi)$  on the  $Z/D = 2.5$  cross stream slice and the location of two pores,  $P1$  and  $P2$  used in convergence analysis. (c) and (d) show the instantaneous, cross stream velocity vectors in the pores labeled  $P1$  and  $P2$ .

A qualitative visualization of the simulation domain and instantaneous flow field is provided in Figure 16. For this Reynolds number and packing geometry, the porescale flow is unsteady, but not turbulent, and is dominated by helical vortices, elongated in the mean flow direction. In their simulations of transitional flows in close packed ordered arrays, Hill and Koch (2002) observed that regions of strong helicity became more pronounced with increasing Reynolds number, up to the limit of unsteadiness. Following their definition, we compute the cosine of the angle between the vorticity and the velocity vectors,

$$\cos(\phi) = \frac{\boldsymbol{\omega} \cdot \mathbf{u}}{\|\boldsymbol{\omega}\| \|\mathbf{u}\|}. \quad (23)$$

Regions with  $\|\cos(\phi)\| \approx 1$  indicate strong helical or corkscrew like trajectories. Instantaneous vortex cores are detected using the swirling strength criteria,  $\lambda_{ci}$  (Zhou et al., 1999), and are visualized as isosurfaces of  $\lambda_{ci}/\lambda_{ci}^{max} = 0.25$  in Figure 16a, where  $\lambda_{ci}^{max}$  is the maximum value of swirling strength in the domain. The surfaces are colored by  $\cos(\phi)$ , indicating the relative orientation and magnitude of helical vortex motion. In Figure 16b, the contours of the  $\cos(\phi)$  field are shown in the cross-stream,  $Z/D = 2.5$  plane. Near the surface of the spheres, and at the exterior wall boundaries, the flow is nearly two dimensional, and  $\cos(\phi)$  is small. In the pores however, regions of  $\cos(\phi) \approx \pm 1$  are dominant. Assuming the velocity and vorticity are directed nominally in the  $+Z$  direction (out of the page), blue regions indicate clockwise helical trajectories ( $\cos(\phi) < 0$ ) and counter-clockwise helical trajectories are indicated by red regions ( $\cos(\phi) > 0$ ). Instantaneous snapshots of the cross-stream vector field in two pores, labeled  $P1$  and  $P2$  are shown in Figures 16c and 16d. The length scale of these vortical structures appears to be roughly  $D/10$  to  $D/20$ , and the magnitude of the cross-stream velocity is on the order of  $1U_p$ . In these vector plots, we also show the location of the line probes used to assess grid convergence of the pore velocity.

The grid convergence of the solution is demonstrated in Figure 17. First, the total hydrodynamic force on the spheres is non-dimensionalized according to equation 15, and plotted as a function of time in Figure 17a for the three different grid resolutions. Both the time average,  $\overline{C_D}$ , as well as the fluctuations in  $C_D$  are sensitive to the grid spacing. Performing a convergence analysis on  $\overline{C_D}$ , using equations 9 and 10, we estimate the order

of convergence to be  $\mathcal{P} = 1.30$ , and determine the uncertainty in the fine grid solution to be  $GCI = 8.24\%$  or  $\overline{C_D} = 245.1 \pm 20.2$ .

The convergence of the time averaged streamwise velocity,  $\overline{u_z}$ , in the  $Z/D = 2.5$  slice is also examined. Averaging over all nodes with monotone convergence (44% of all nodes in the post processing grid), the globally averaged observed convergence rate for this quantity is  $\mathcal{P}_G = 3.3$ . This is above the formal order of accuracy of the code, and could be due to the  $\Delta = D/40$  solution being out of the asymptotic convergence range in some regions. Using this convergence rate results in a globally averaged uncertainty of  $GCI_G = 5\%$  of  $RMS(\overline{u_z})$ .

Because of the randomness of the bed, certain regions of the porespace are more grid converged than others. This is demonstrated by the velocity profiles extracted from pores  $P1$  and  $P2$  which are plotted in Figure 17b and Figure 17c. The line probe through pore  $P1$ , along the line  $X/D = 0.16$ ,  $Z/D = 2.5$  demonstrates good convergence and low uncertainty for  $\Delta = D/80$ . In fact, the only slight differences in the solution on all three grids seems to be near the counter-rotating helical features between  $Y/D = 2$  and  $Y/D = 2.5$ . The probe in the  $P2$  pore along the line  $Y/D = 1.85$ ,  $Z/D = 2.5$  indicates larger uncertainties and worse overall convergence. We believe that the randomness of the bed could be the cause of this behavior. Slight shifts in mean flow upstream of this plane for example could propagate non-linearly downstream. This was not an issue when examining the results for structured packings (Section 3.4), but should certainly be a consideration when performing resolved simulations of random arrangements. Nonetheless, the major features of the velocity profile along the line, including a maximum near  $X/D = 2.1$  and minima near  $X/D = 1.7$  and  $X/D = 2.6$ , are consistent across the three grids.

The statistical nature of the porescale flow has been examined by plotting the PDFs of the instantaneous velocity components as well as  $\cos(\phi)$  for one instant in time in the porespace ( $0.5 < Z/D < 3.5$ ). In Figure 18 the PDF of each of the velocity components is shown. The PDFs have been normalized to have a standard deviation of one, for comparison with the Gaussian distribution, plotted as a solid line, and with the lattice Boltzmann simulations of Hill and Koch (2002) for structured close-packings. Similar to their study, there is a peak in the PDF of each velocity component for  $u_i = 0$ , corresponding to the large amount of fluid

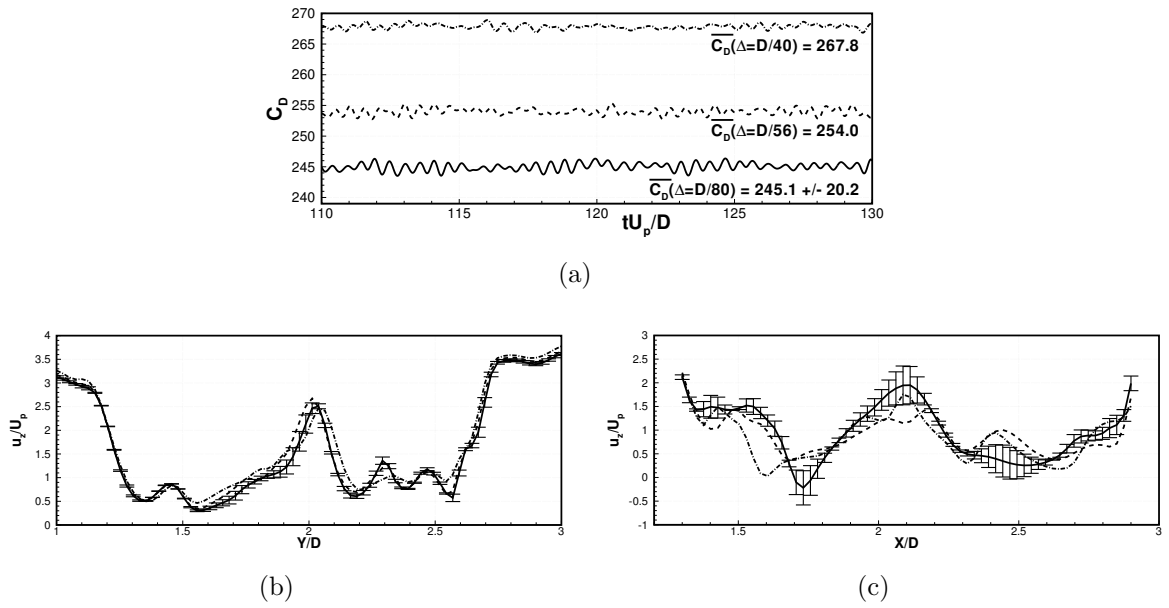


Figure 17: Grid convergence analysis for the randomly packed bed. (a) Time history of the drag coefficient. (b) Time averaged streamwise velocity,  $\overline{u_z}$  non-dimensionalized by  $U_P$  in pore  $P1$ , along the line  $X/D = 0.16$ ,  $Z/D = 2.5$ . (c) Same as (b) but along the line  $Y/D = 1.85$ ,  $Z/D = 2.5$  in pore  $P2$ .

influenced by the solid boundaries. The cross stream components have a nearly Gaussian spread, but with wider tails at high velocity. In comparison, Hill and Koch observed tails with less spread than the normal distribution. This difference is likely due the high void fraction of the present sphere packing which can accommodate larger cross-stream fluid motion relative to the structured close packing. The PDF of the streamwise component,  $u_z$  indicates that a significant portion of fluid, about 7%, is directed upstream, also similar Hill and Koch’s observations. The PDF of  $\cos(\phi)$ , shown in Figure 19, corresponds well with their results. The peak at 0 is due to the strong influence of the walls, near which the flow is two dimensional, even at this relatively high Reynolds number. The symmetric tails of the PDF, with peaks at  $\pm 1$  show the high degree of strong helical motion in the porespace.

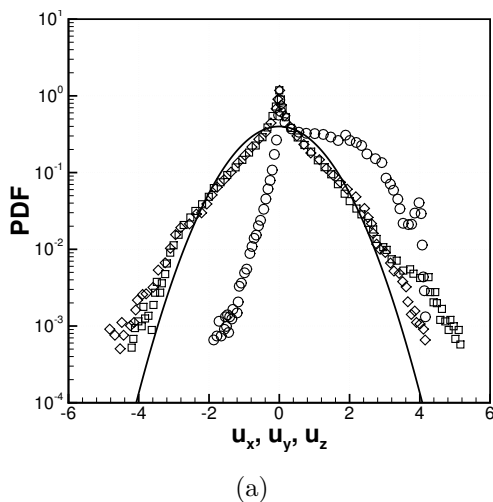
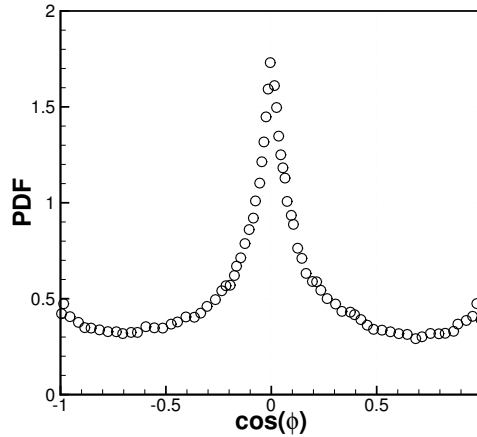


Figure 18: Normalized probability distribution function of the velocity components in the porespace for flow through the random packing.  $\diamond u_x$ ,  $\square u_y$ ,  $\circ u_z$ , — Gaussian distribution with zero mean and standard deviation of one.

## 6. Conclusions

The performance of a fictitious domain approach relative to a body fitted approach has been assessed for simulation of flow through packed beds of spheres. The body-fitted approach utilizes a cylinder bridge model during mesh generation to avoid troublesome sphere



(a)

Figure 19: Probability distribution function of the cosine of the angle between the velocity and vorticity vectors in the porespace for flow through the random packing.

to sphere contact points. This strategy avoids major modification of the solid geometry and removes areas where small elements are required. The main advantage of the fictitious domain approach for fixed bed and porous media problems is that it can use regular Cartesian grids, and avoids unstructured mesh generation all together. In this case, the solid-fluid interface is accurately represented using Lagrangian marker points with subgrid resolution, and a rigidity constraint within the solid bodies is imposed to enforce the no-slip boundary condition.

Several test cases have been examined to address particular concerns associated with simulating flow in packed beds. It was first shown using decaying Taylor vortices that local grid quality issues can result in a significant increase in solution error, even for only mildly skewed cells. This is an important point to consider for packed bed simulations because in large scale random packings, some skewed elements are inevitable when creating a body fitted mesh. Next, the case of Stokes flow in a dilute periodic array was used as a basic hydrodynamic validation case relevant to packed beds, without having to consider sphere to sphere contact points. Using the case of two contacting spheres, it was shown that for moderate Reynolds numbers the region of fluid very close to the contact point has little effect on the bulk flow, and may be safely removed as is deliberately done in the bridge

meshing technique. This is also reassuring for the fictitious domain technique, which can only resolve sphere to sphere contact points at the scale of the Cartesian mesh. **By observing the grid convergence of the total drag coefficient in this case, it was confirmed that the body fitted and fictitious domain surface representations are very nearly equivalent for contacting sphere geometries.** The final test case considered, flow through a section of a simple cubic lattice, allowed us to perform a detailed comparison of both methods in a prototypical sphere packing. In this case, a systematic grid refinement study has been performed, with the grid convergence index (GCI) used to assess uncertainty of the fine grid solutions. Both methods perform well at steady flow rates ( $Re = 12, 105, 204$ ) in the sense that they predict interstitial velocity profiles in agreement with the experimental data of Suekane et al. (2003). The difference is that fictitious domain approach is able to obtain a solution with low uncertainty using a much lower grid density than the body fitted approach. Similar trends are observed for the unsteady flow rates ( $Re = 450, 600$ ). In these cases, the body fitted approach is observed to have large uncertainty associated with the TKE distribution, making it undesirable for use at higher Reynolds numbers.

The scalability of both approaches for general, random packed bed flow simulations has been estimated. For a predetermined target level of uncertainty the computational expense, estimated to be proportional to the number of control volumes times the number of timesteps, is found to be between 1.9 and 65 times more for the body fitted approach compared to the fictitious domain approach for the cases considered. Actual CPU timings for the periodic SCP channel indicate that speedup may be more modest, perhaps 5 times. Finally, the fictitious domain approach has been applied to a more practical case of unsteady flow at  $Re = 600$  through a random packing of 51 spheres. The results show grid convergence in global and local time averaged quantities, although the randomness of the packing results in significant variation in the local uncertainties. Nonetheless, results capture complex instantaneous porescale flow features and are used to further explore helical motions in random arrangements. Good statistical agreement is obtained with prior Lattice Boltzmann results of Hill and Koch (2002).

## 7. Acknowledgments

This work was supported by the National Science Foundation (Project #0933857: *Inertial Effects in Flow Through Porous Media*). Many of the larger simulations were performed on the Lonestar supercomputer at the Texas Advanced Computing Center. We thank the anonymous reviewers for thoughtful comments and suggestions which led to a number of improvements.

- Andrigo, P., Bagatin, R., Pagani, G., 1999. Fixed bed reactors. *Catalysis today* 52 (2-3), 197–221.
- Apte, S., Martin, M., Patankar, N., 2009. A numerical method for fully resolved simulation FRS of rigid particle-flow interactions in complex flows. *Journal of Computational Physics* 228 (8), 2712–2738.
- Atmakidis, T., Kenig, E., 2009. CFD-based analysis of the wall effect on the pressure drop in packed beds with moderate tube/particle diameter ratios in the laminar flow regime. *Chemical Engineering Journal* 155 (1), 404–410.
- Cadafalch, J., Pérez-Segarra, C., Consul, R., Oliva, A., 2002. Verification of finite volume computations on steady-state fluid flow and heat transfer. *Journal of Fluids Engineering* 124, 11–21.
- Calis, H., Nijenhuis, J., Paikert, B., Dautzenberg, F., Van Den Bleek, C., 2001. CFD modelling and experimental validation of pressure drop and flow profile in a novel structured catalytic reactor packing. *Chemical Engineering Science* 56 (4), 1713–1720.
- Cardenas, M., Wilson, J., 2007. Dunes, turbulent eddies, and interfacial exchange with permeable sediments. *Water Resources Research* 43 (8), W08412.
- Celik, I., Ghia, U., Roache, P., et al., 2008. Procedure for estimation and reporting of uncertainty due to discretization in CFD applications. *Journal of Fluids Engineering-Transactions of the ASME* 130 (7).
- Dixon, A., Nijemeisland, M., Stitt, E., 2006. Packed tubular reactor modeling and catalyst design using computational fluid dynamics. *Advances in Chemical Engineering* 31, 307–389.
- Dong, H., Bozkurtas, M., Mittal, R., Madden, P., Lauder, G., 2010. Computational modelling and analysis of the hydrodynamics of a highly deformable fish pectoral fin. *Journal of Fluid Mechanics* 645, 345–373.
- Dybbs, A., Edwards, R., 1984. A new look at porous media fluid mechanics—Darcy to turbulent. *Fundamentals of Transport Phenomena in Porous Media*, 199–254.
- Eça, L., Hoekstra, M., Roache, P., 2005. Verification of calculations: An overview of the Lisbon workshop. In: *23rd AIAA Applied Aerodynamics Conference*. pp. 1–12.
- Ergun, S., 1952. Fluid flow through packed columns. *Chem. Eng. Prog* 48 (2), 89–94.
- Falgout, R., Yang, U., 2002. hypre: A library of high performance preconditioners. *Computational Science-ICCS 2002*, 632–641.

- Finn, J., Apte, S., 2012. Characteristics of vortical structures in random and arranged packed beds of spheres. Proceedings of the ASME Fluids Engineering Summer Meeting (FEDSM2012-72354).
- Glowinski, R., Pan, T., Hesla, T., Joseph, D., Periaux, J., 2001. A fictitious domain approach to the direct numerical simulation of incompressible viscous flow past moving rigid bodies: application to particulate flow. *Journal of Computational Physics* 169 (2), 363–426.
- Guardo, A., Coussirat, M., Recasens, F., Larrayoz, M., Escaler, X., 2006. CFD study on particle-to-fluid heat transfer in fixed bed reactors: Convective heat transfer at low and high pressure. *Chemical Engineering Science* 61 (13), 4341–4353.
- Gunjal, P., Ranade, V., Chaudhari, R., 2005. Computational study of a single-phase flow in packed beds of spheres. *AIChE Journal* 51 (2), 365–378.
- Haeri, S., Shrimpton, J., 2012. On the application of immersed boundary, fictitious domain and body-conformal mesh methods to many particle multiphase flows. *International Journal of Multiphase Flow* 40, 38–55.
- Ham, F., Apte, S., Herrmann, G. C., Mahesh, K., Moin, P., 2003. Unstructured LES of reacting multiphase flows in realistic gas turbine combustors. *Annual Research Briefs-2003*, 139.
- Ham, F., Iaccarino, G., 2004. Energy conservation in collocated discretization schemes on unstructured meshes. *Center for Turbulence Research Annual Research Briefs*, 3–14.
- Hill, R., Koch, D., 2002. The transition from steady to weakly turbulent flow in a close-packed ordered array of spheres. *Journal of Fluid Mechanics* 465, 59–97.
- Huang, A., Huang, M., Capart, H., Chen, R., 2008. Optical measurements of pore geometry and fluid velocity in a bed of irregularly packed spheres. *Experiments in Fluids* 45 (2), 309–321.
- Kim, D., Choi, H., 2000. A second-order time-accurate finite volume method for unsteady incompressible flow on hybrid unstructured grids. *Journal of Computational Physics* 162 (2), 411–428.
- Kuroki, M., Ookawara, S., Ogawa, K., 2009. A high-fidelity CFD model of methane steam reforming in a packed bed reactor. *Journal of Chemical Engineering of Japan* 42 (Supplement.), 73–78.
- Magnico, P., 2003. Hydrodynamic and transport properties of packed beds in small tube-to-sphere diameter ratio: pore scale simulation using an eulerian and a lagrangian approach. *Chemical Engineering Science* 58 (22), 5005–5024.
- Magnico, P., 2009. Pore-scale simulations of unsteady flow and heat transfer in tubular fixed beds. *AIChE Journal* 55 (4), 849–867.
- Mahesh, K., Constantinescu, G., Moin, P., 2004. A numerical method for large-eddy simulation in complex geometries. *Journal of Computational Physics* 197 (1), 215–240.
- Malico, I., Ferreira de Sousa, P., 2012. Modeling the pore level fluid flow in porous media using the immersed boundary method. *Numerical Analysis of Heat and Mass Transfer in Porous Media*, 229–251.

- Moin, P., Apte, S., 2006. Large-eddy simulation of realistic gas turbine-combustors. *AIAA Journal* 44, 698–708.
- Nelson, B., 2009. Scaling analysis for the pebble bed of the very high temperature gas-cooled reactor thermal hydraulic test facility. Ph.D. thesis, Oregon State University.
- Nijemeisland, M., Dixon, A., 2004. CFD study of fluid flow and wall heat transfer in a fixed bed of spheres. *AICHE journal* 50 (5), 906–921.
- Ovaysi, S., Piri, M., 2010. Direct pore-level modeling of incompressible fluid flow in porous media. *Journal of Computational Physics* 229 (19), 7456–7476.
- Patankar, N., Joseph, D., 2001. Modeling and numerical simulation of particulate flows by the Eulerian-Lagrangian approach. *International Journal of Multiphase Flow* 27 (10), 1659–1684.
- Patil, V., Liburdy, J., 2012. Optical measurement uncertainties due to refractive index mismatch for flow in porous media. *Experiments in Fluids* 53 (5), 1453–1468.
- Peskin, C., 1972. Flow patterns around heart valves: A digital computer method for solving the equations of motion. Ph.D. thesis, Sue Golding Graduate Division of Medical Sciences, Albert Einstein College of Medicine, Yeshiva University.
- Peskin, C., 1977. Numerical analysis of blood flow in the heart. *Journal of Computational Physics* 25 (3), 220–252.
- Roache, P., 1994. Perspective: a method for uniform reporting of grid refinement studies. *Journal of Fluids Engineering-Transactions of the ASME* 116 (3), 405–413.
- Roache, P., 1997. Quantification of uncertainty in computational fluid dynamics. *Annual Review of Fluid Mechanics* 29 (1), 123–160.
- Roache, P., 2003. Conservatism of the grid convergence index in finite volume computations on steady-state fluid flow and heat transfer. *Journal of Fluids Engineering-Transactions of the ASME* 125 (4), 731–732.
- Robbins, D., El-Bachir, M., Gladden, L., Cant, R., von Harbou, E., 2012. CFD modeling of single-phase flow in a packed bed with MRI validation. *AICHE Journal*.
- Roma, A. M., Peskin, C. S., Berger, M. J., 1999. An adaptive version of the immersed boundary method. *Journal of computational physics* 153 (2), 509–534.
- Sharma, N., Patankar, N., 2005. A fast computation technique for the direct numerical simulation of rigid particulate flows. *Journal of Computational Physics* 205 (2), 439–457.
- Simeonov, J., Calantoni, J., 2011. A pressure boundary integral method for direct fluid-particle simulations on Cartesian grids. *Journal of Computational Physics* 230 (5), 1749–1765.
- Smolarkiewicz, P., Larrabee Winter, C., 2010. Pores resolving simulation of Darcy flows. *Journal of Computational Physics* 229 (9), 3121–3133.
- Suekane, T., Yokouchi, Y., Hirai, S., 2003. Inertial flow structures in a simple-packed bed of spheres. *AICHE*

- Journal 49 (1), 10–17.
- Taylor, G., 1923. On the decay of vortices in a viscous fluid. *Phil. Mag* 46 (6), 671–674.
- Uhlmann, M., 2005. An immersed boundary method with direct forcing for the simulation of particulate flows. *Journal of Computational Physics* 209 (2), 448–476.
- Vargas, A., Mittal, R., Dong, H., 2008. A computational study of the aerodynamic performance of a dragonfly wing section in gliding flight. *Bioinspiration & Biomimetics* 3, 026004.
- Wood, B., 2007. Inertial effects in dispersion in porous media. *Water Resources Research* 43 (12), 12.
- Zhou, J., Adrian, R., Balachandar, S., Kendall, T., 1999. Mechanisms for generating coherent packets of hairpin vortices in channel flow. *Journal of Fluid Mechanics* 387 (1), 353–396.
- Zhu, L., Peskin, C., 2002. Simulation of a flapping flexible filament in a flowing soap film by the immersed boundary method. *Journal of Computational Physics* 179 (2), 452–468.
- Zick, A., Homsy, G., 1982. Stokes flow through periodic arrays of spheres. *Journal of Fluid Mechanics* 115, 13–26.